International Journal of Solids and Structures 267 (2023) 112163

Contents lists available at ScienceDirect

International Journal of Solids and Structures

journal homepage: www.elsevier.com/locate/ijsolstr

Thermo-mechanical properties of digitally-printed elastomeric polyurethane: Experimental characterisation and constitutive modelling using a nonlinear temperature-strain coupled scaling strategy

Jie Yang [a,b,1], Zisheng Liao [a,b,1], Mokarram Hossain [b,*], Guanyu Huang [a], Xin Zhou [d], Fan Liu [a], Ahmed S.M. Alzaidi [c], Xiaohu Yao [a,*]

[a] State Key Laboratory of Subtropical Building Science, South China University of Technology, Guangzhou 510640, China
[b] Zienkiewicz Centre for Computational Engineering (ZCCE), Faculty of Science and Engineering, Swansea University, Swansea, SA1 8EN, United Kingdom
[c] Department of Mathematics and Statistics, College of Science, Taif University, P.O. Box 11099, Taif 21944, Saudi Arabia
[d] South China Advanced Institute for Soft Matter Science and Technology, South China University of Technology, Guangzhou 510640, China

ARTICLE INFO

Keywords:
Additive manufacturing
Digitally-printed polyurethane
Experimental characterisation
Constitutive modelling
Temperature effect

ABSTRACT

The Additive manufacturing (AM) technology has emerged as a novel paradigm that uses the method of gradual accumulation of materials to manufacture solid parts, which is a "bottom-up" approach compared to the traditional cutting technology. Among available techniques, Digital Light Synthesis (DLS) further facilitates the opportunity for continuous building instead of the layer-by-layer or the dot-by-dot printing approach, thus curtailing the time of production and encouraging the development of many new materials. In this contribution, temperature-dependent mechanical properties of a DLS-based 3D-printed elastomeric polyurethane (EPU) are investigated by utilising experimental characterisation and constitutive modelling. Specifically, uniaxial tensile and stress relaxation tests under temperature fields ranging from −20 °C to 60 °C are performed, which reveal deformation-nonlinearity and temperature-sensitivity of the elastomer. This temperature range covers the glass transition of the polymer. Experimental results show that the temperature-dependence is also correlated with strain levels. Motivated by the experimental results, a phenomenologically-inspired thermodynamically-consistent constitutive model is formulated to characterise the finite deformation behaviours of EPU. In this case, for the first time, a single temperature-strain coupled function can capture the thermo-mechanical behaviour across the glass transition. Satisfactory accuracy of the prediction can be seen using the proposed constitutive model. This study contributes to the fundamental understanding of the mechanical properties of DLS-based digitally-printed EPU under a wide temperature field. The comprehensive thermo-mechanical experimental characterisation and subsequent constitutive modelling will facilitate the designing of other 3D-printed soft materials.

1. Introduction

Polyurethane (PU) is a broad range of polymeric materials which have analogous structures as illustrated in Fig. 1. They are widely used in many engineering applications including paints, liquid coating, adhesives, etc (Akindoyo et al., 2016; Chattopadhyay and Raju, 2007; Krol, 2007; Petrović and Ferguson, 1991; Rafiee and Keshavarz, 2015; Wang et al., 2017). Considering the differences in raw materials during their synthesis processes, PU has various forms such as porous form and plastic sponge. Among PU, elastomeric polyurethane (EPU), a soft polymer, has excellent tear strength, low wave speeds, strong impact resistance, and a low glass transition temperature (Zhang et al., 2015a; Chattopadhyay and Raju, 2007; Somarathna et al., 2020a). As a result, EPU has become increasingly popular in many engineering fields such as low-speed tyres (Akindoyo et al., 2016; Petrović and Ferguson, 1991) and the interlayer of windshields (Zhang et al., 2015c,b,d; Liao et al., 2019). As displayed in Fig. 1, a two-domain conformation can be seen in the monomers of EPU. The hard segments tend to aggregate due to the easily formed hydrogen bonds, whilst the soft segments

* Corresponding authors.
E-mail addresses: ctjyang@mail.scut.edu.cn (J. Yang), l.zisheng@mail.scut.edu.cn (Z. Liao), mokarram.hossain@swansea.ac.uk (M. Hossain), ctgyhuang@mail.scut.edu.cn (G. Huang), 202020160126@mail.scut.edu.cn (X. Zhou), 201710101159@mail.scut.edu.cn (F. Liu), azaidi@tu.edu.sa (A.S.M. Alzaidi), yaoxh@scut.edu.cn (X. Yao).
[1] The authors contributed equally to this work.

https://doi.org/10.1016/j.ijsolstr.2023.112163
Received 3 October 2022; Received in revised form 6 February 2023; Accepted 12 February 2023
Available online 16 February 2023

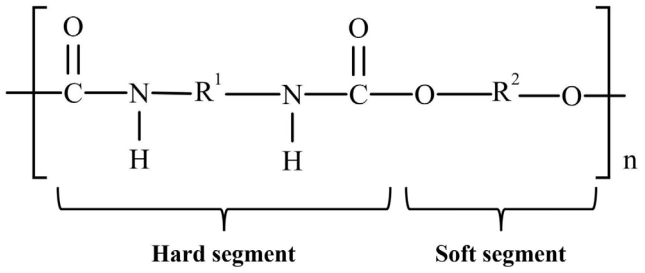

Fig. 1. The chemical formula of PU consisting of a hard segment and a soft segment. R^1 and R^2 represent different chemical structures from isocyanate and polyols, respectively. Note that hydrogen bonds are easily formed between "N–H" and "C=O", which results in the aggregation phenomenon of hard domains commonly seen in PU.

function as the flexible continuous matrix in which hard domains intersperse (Zhang et al., 2018). As a result of the aggregation phenomenon, hard segments act as the net points to stabilise the chain segment network, and soft segments serve as the molecular switches due to the crystalline characteristics of the amorphous domains (Park et al., 2021). Besides, the aggregated hard domains of EPU serving as the additions may affect the deformation pattern of the amorphous matrix (Yang et al., 2021). The results of Arman et al. (2012) showed that this kind of multi-block architecture of EPU could increase energy dissipation and reduce shock velocity.

The additive manufacturing (AM) has emerged as a cutting-edge digital manufacturing technology across a variety of fields of engineering sciences. Although significant strides have been made in hard material printing, the applications for 3D-printed soft polymers are still few and most parts being printed using the conventional layer-by-layer or dot-by-dot printing strategies, e.g., Inkjet Printing (IP), Stereolithography (SLA), and Digital Light Projection (DLP) (Hossain and Liao, 2020). Compared to these existing time-consuming AM methods, the invention of the Digital Light Synthesis (DLS) streamlines the AM process of many soft materials (Tumbleston et al., 2015). In particular, the DLS technique enables continuous construction, which has a revolutionary effect on the technology of quick prototyping and structural integration, thus encouraging the development of many new materials (Abali and Barchiesi, 2021; Hossain and Liao, 2020; Tumbleston et al., 2015; Ligon et al., 2017; Stansbury and Idacavage, 2016). Complex three-dimensional geometric designs that are challenging to achieve in traditional machining industries using cutting-like technologies, may now be completed with high efficiency and great precision thanks to the DLS technology. Compared with traditional polymer, 3D printing polymer owes less void volume and enhanced mechanical and physical properties (Christ et al., 2018). In the past decade, soft material has accounted for roughly half of the additively manufactured materials (Associates, 2016). This technology has applications in architecture, medicine, automotive, flexible electronics, sensors, etc (Ligon et al., 2017; Stansbury and Idacavage, 2016; Slesarenko and Rudykh, 2018; Unkovskiy et al., 2018; Xiao et al., 2021; Christ et al., 2017, 2018), and is currently attracting unprecedented interest from industry and academia alike. It should be noted that the material properties have a strong tunability in the 3D printing process because of two main reasons: the controllability of the printing process and the convenience of the incorporation of other materials. Many effects such as light intensity (Xiang et al., 2020; Yu et al., 2019), oxygen (Zhao et al., 2015), UV-curing (Kim et al., 2017), and filler content (Christ et al., 2018, 2017; Vyas et al., 2022; Zhou et al., 2022) on the material properties have been investigated for 3D-printed polymers.

EPU has been synthesised very early using traditional manufacturing techniques such as injection moulding and has a high yield and applications in recent years. EPU is subjected to a wide variety of temperature fluctuation, many loading–unloading cycles, and extreme conditions during its service life, primarily in the tension mode of deformation (Larcher et al., 2012). Hence, experimental investigations are crucial in gaining a complete understanding of this soft polymeric material. For instance, Petrović and Ferguson (1991) conducted detailed tests as early as 1991. Several static experiments were carried out by Nikoukalam and Sideris (2019), including cyclic loading, relaxation, and creep compressive tests. Therein, the effects of nonlinearity in the stress–strain relationships, rate sensitivity, monotonic-cyclic damage, and hysteresis were thoroughly studied. Qi and Boyce (2005a) and Qi (2004) studied the compressive mechanical characteristics of EPU at room temperature under low to intermediate strain rates (less than 100 /s). Furthermore, temperature-sensitive behaviour has also been considered in a few studies. For instance, Amirkhizi et al. (2006) established temperature and pressure correlations of polyurea (a kind of soft polymer with similar mechanical properties to EPU) by performing Hopkinson bars with and without confining pressure from 0 °C to 40 °C. Gong et al. (2021) conducted a series of uniaxial compression studies from −30 °C to 60 °C. Their findings show extreme nonlinearity, temperature-sensitivity, and rate-sensitivity of polyurea. Zhang et al. (2015c) studied the temperature effect from −40 °C to 50 °C of EPU. Further, Liao et al. (2019) and Zhang et al. (2015c) revealed the viscoelastic properties of the same material by carrying out quasi-static cyclic tests, large tensile deformation, and fracture tests. The temperature of their experiments ranged from −40 °C to 40 °C. A considerable impact on the mechanical properties from strain rate and temperature has been found on the tensile and failure behaviours in their studies. Experiments conducted under a temperature field indicated that as the temperature is decreased, EPU tends to transform from a rubbery state to a glassy state (i.e., Glass Transition). The specific transition temperature is called the glass transition temperature (T_g). Strain rate also has a similar effect (Liao et al., 2019; Yi et al., 2006; Sarva et al., 2007; Guo et al., 2016). This synergistic relationship is known as the Time–Temperature Superposition (TTS) principle, which has been extensively studied in Zhang et al. (2015a,c), Liao et al. (2019) and Pramanik et al. (2022).

Several constitutive models have been proposed over the years for replicating the experimental results to explore the mechanical properties of EPU. For example, Amirkhizi et al. (2006) employed a linear viscoelastic model modified by the TTS principle to reveal the pressure and temperature dependence of polyurea. Furthermore, based on two viscoelastic rheology elements, Shim and Mohr (2011) put forward a compressive model of polyurea. Multi-step loading–unloading relaxation paths can be reproduced by their model. Zhang et al. (2017) used a step-wise phenomenological model to reveal the time–temperature–pressure dependency of polyurea. Nantasetphong et al. (2016) devised a modified Williams–Landel–Ferry (WLF) equation that could reproduce the pressure effect of confined compression tests of polyurea. Based on the classic micromechanical-based eight-chain hyperelastic model (Arruda and Boyce, 1993), Qi and Boyce (2005a) incorporated the concept of strain amplification driven by the evolution of soft domain volume fraction to capture the stress softening behaviour of EPU. Other investigations on the hyperelastic properties of EPU can also be seen in Jiao et al. (2009), Wang et al. (2020), Ding et al. (2021), Rull et al. (2021), Somarathna et al. (2020b) and Grujicic et al. (2011). Exploring the rheological concepts, many studies also focus on the viscoelasticity of EPU. To complement the compressive experiment results of EPU at room temperature and low strain rates, Qi and Boyce (2005a) and Qi (2004) built a viscoelastic constitutive model. Shim and Mohr (2011) investigated the multi-step loading–unloading relaxation behaviour of polyurea using a compressive model of two viscoelastic rheology elements. Clifton et al. (2016) presented a pressure-dependent physically-based integral form of viscoelastic constitutive law of polyurea for modelling flyer plate response. Some viscoelastic–viscoplastic coupled constitutive models for polyurea and EPU can be found in the literature (Cho et al., 2013; Nikoukalam and Sideris, 2019; Yuan et al., 2020). However, mere studies have focused on the temperature sensitivity on soft materials in their theoretical model (Zhang et al.,

2015c; Amirkhizi et al., 2006; Nantasetphong et al., 2016). Despite a wide range of studies combining experiments and modelling either for polyurea or EPU made from traditional manufacturing processes such as injection moulding, to the best of the authors' knowledge, there is no thermo-mechanical study meeting computational model for the 3D-printed EPU. Very recently, a viscoelastic constitutive model for EPU manufactured by the DLS technology was developed by Hossain et al. (2020) in which temperature effects were discarded. There are also few studies on the constitutive modelling for 3D-printed polymers and polymer printing processes (Garzon-Hernandez et al., 2020b,a). Xiang et al. (2020) printed the specimens at different light intensities, and their results show that the viscous stress and the viscosity would increase upon the increase of the light intensity. They accordingly developed an intensity-dependent visco-hyperelastic model of photocured polymers. In their assumption, the high light intensities would increase the density and number of crosslinked networks, which rationalises the light sensitivity of photocured polymers. Yu et al. (2019) developed a constitutive model to theoretically investigate the influence of light intensity, light wavelength, and photo-initiator concentration on the self-healing phenomenon of optically healable polymers. They successfully predict that the interfacial self-healing strength of the polymer would increase with the increase of light illumination time and the light intensity and the decrease of wavelength until reaching a plateau.

Overall, there is currently a lack of complete mechanical properties analysis of 3D-printed EPU over a wide range of temperature that undergoes the glass transition. Furthermore, corresponding constitutive models incorporating temperature beyond and across the glass transition temperature are rare. The wide range of applications for 3D-printed EPU necessitate a thorough understanding of its mechanical properties. For characterising the thermo-mechanical properties of EPU, temperature experiments are carried out in this contribution. Afterwards, a thermo-hyper-viscoelastic constitutive model has also been built based on the thermodynamical principles of continuum mechanics to further understand the material. As in the validation section, the constitutive model shows a good agreement with the experimental results. This study contributes to the fundamental understanding of the mechanical properties of 3D-printed EPU under a wide temperature range.

The following is a breakdown of the structure of this manuscript. In addition to the current section, Section 2 specifies the details of experiments, and the corresponding results and discussions can be seen in Section 3. In Section 4, a phenomenological thermo-hyper-viscoelastic constitutive model is built based on continuum mechanics and thermo-dynamics. Finally, we present a summary of the results and conclusions in Section 5.

2. Experiments

2.1. Specimen preparation

Similar to our previous studies (Hossain et al., 2020; Hossain and Liao, 2020), specimens are synthesised by a DLS-based printer (Model: Carbon3D M2, see Fig. 2(a)). In addition, Fig. 2(b) presents a schematic diagram to describe the basic features of this technology which is reproduced here for clarity. As seen in Fig. 2(b), the DLS technology is a continuous printing method using ultraviolet (UV) light for the material curing through an oxygen-permeable window that has high optical clarity and an extremely low refractive index. Between this window and the 3D printing part, there is a thin layer made of uncured resin known as the dead-zone (a region devoid of oxygen) to prevent the part from sticking to the uncured part and to permit a continuous flow of liquid resins underneath the part (Stansbury and Idacavage, 2016). The directionality-sensitivity may be the characteristics of few 3D printing processes because of the existence of machine direction alignment. However, for the vat-polymerisation process such as the Digital Light Synthesis (DLS) used here in this study, the 3D printing of a polymer layer happens as a whole in which the light is projected on the entire layer. Hence, the printing directional-related sensitivity is minimal to the mechanical properties, see Al Rashid et al. (2021) and Christ et al. (2018).

The specimen size employed in our experiments is illustrated in Fig. 3. To avoid breaking at the clip position, a flat dumbbell shape is chosen, which can also be seen in many experimental studies (Zhang et al., 2015c; Liao et al., 2019). The gauge portion has a 50 mm length, a 5 mm width, and a 3 mm thickness. The fillet radius is set to be 5 mm. Before being mounted on the grippers, the specimens are glued to aluminium shims to ensure a tight grasp and avoid the slippage of the clamping parts.

2.2. Equipments and test schedules

Before conducting any tensile experiments under temperature conditions, T_g must be determined to assist in defining the temperature range used in our experiments. For this, Dynamic Mechanical Analysis (DMA) is a useful method. Under alternating deformation, the dynamic modulus information including Loss Tangent ($\tan\delta$) of the material is measured. The DMA experiments are performed utilising a Dynamic Mechanical Analyser (Model: **DMA 242E Artemis** manufactured by the NETZSCH company in Germany) and the experimental schedule is listed in Table 1. Note that the peak temperature of $\tan\delta$ curve is used as T_g here.

Tensile experiments are carried out using an Instron 5567 Universal Test Machine (see Fig. 4) equipped with a force sensor (± 500 N). To control the temperature stability, all experiments are conducted in a bespoke temperature chamber. Before each test begins, specimens are placed in the temperature chamber for half an hour to minimise the temperature discrepancies. Nominal stress and nominal strain are used to record the experimental results. Note that the nominal strain is measured as the crosshead (seen in Fig. 4) displacement divided by the initial length of the specimen (50 mm). The schedule of uniaxial loading–unloading tension experiments and stress relaxation experiments are described in Table 2. In addition, to confirm the reproducibility, each condition is repeated at least three times, and the error bars are added to show the standard deviation of the results. For the uniaxial tension experiments, three different strain rates of 0.1 /s, 0.01 /s, and 0.001 /s and a wide temperature range of −20 °C to 60 °C (determined by the T_g value) are considered. As seen in the following results, the selected temperature range spans T_g and the glass transition phenomenon is observed at this temperature range. It should be noted that in our experiments, the changes in the gauge length due to the temperature variation have been omitted as they are small. Besides, according to trial experiments, this material fails at a strain of around 300% strain. Hence, to avoid the failure due to vitrification under low-temperature cases, the strain levels are chosen as 100%, 150%, and 200%. In terms of the single-step stress relaxation experiments, each specimen is stretched at 0.1 /s and then held at the desired strain of 200% for 6000 s. In addition, multi-step relaxation experiments are carried out with 0.1 /s loading rate and with one-hour relaxation at every 25% strain interval. The maximum strain for the multi-step relaxation experiments is 200%.

3. Experimental results and discussion

3.1. Glass transition temperature

The $\tan\delta$ curve at 1 Hz over −40 °C to 100 °C is depicted in Fig. 5 which clearly demonstrates temperature-sensitivity phenomena of the material. The line peaks at 8.8 °C which is used as T_g in this contribution. In the following sections, we select four typical temperatures, i.e., −20 °C, 0 °C, 20 °C, and 60 °C for the mechanical tests. The glass transition phenomenon can be seen under the temperature range that is chosen here.

Table 1
Experimental schedule of DMA test.

Experiment name	Gauge section size [mm]	Temperature range [°C]	Heating rate [°C/min]	Displacement amplitude [mm]	Frequency [Hz]
DMA	4 × 5 × 3	−40~100	5	0.05	1

Table 2
Experimental schedules under different temperature conditions.

Deformation mode	Strain rate [/s]	Holding time [s]	Strain levels [%]	Temperature [°C]			
				−20	0	20	60
Uniaxial tension	0.001	–	200	–	–	•	–
	0.01	–	200	–	–	•	–
	0.1	–	100, 150, 200	•	•	•	•
Single-step stress relaxation	0.1	6000	200	•	•	•	•
Multi-step stress relaxation	0.1	3600	25, 50, … ,200	–	–	•	–

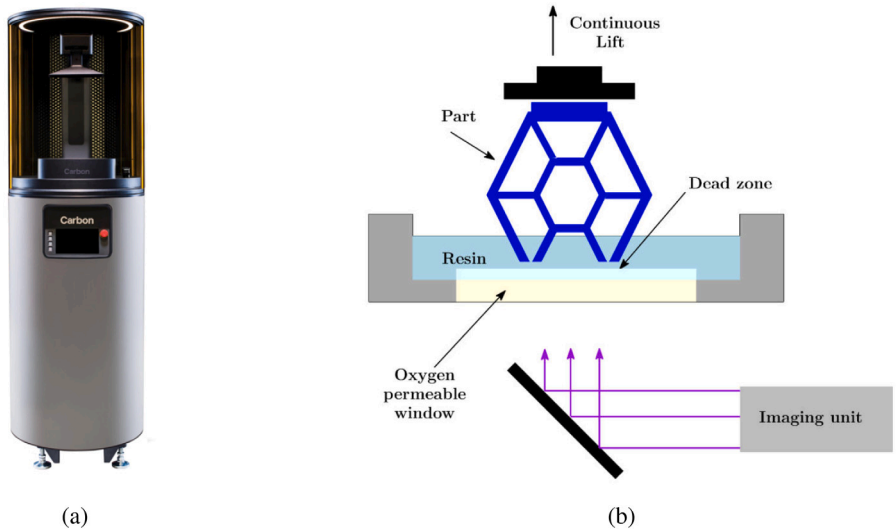

Fig. 2. (a) The DLS-based 3D printer CarbonM2 and (b) a schematic diagram of the DLS technology (Hossain and Liao, 2020).

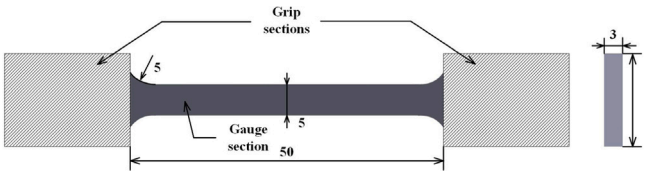

Fig. 3. The specimen size employed in our experiments. The gauge portion has a 50 mm length, a 5 mm width, and a 3 mm thickness. The flat dumbbell shape is adopted to avoid breakage at the clip position, since the stress state is complex here.

3.2. Loading–unloading cyclic tests

The results of loading–unloading experiments at different maximum strain levels are presented in Fig. 6. The inset depicts the strain controlling paths over time on the normal axis. By a linear fitting of the initial loading part, Young's modulus is identified to be 13.26 ± 1.52 MPa under 0.1 /s and 20 °C. For the cases of different maximum strain levels, the loading paths are nearly identical, whilst hysteresis and residual strain levels increase with higher maximum strain levels. The loading–unloading cyclic tests are also carried out under different strain rates, i.e., 0.1 /s, 0.01 /s, and 0.001 /s, as shown in Fig. 7. The inset depicts the strain controlling paths over time on the logarithmic axis. Note that, since the high rate cases are not included, e.g., 500 /s, the glass transition arising from the high strain rate cannot be observed in our results. Stress only shows a linear shift in response to the variation of the rates at low strain rates. However, the strain rates we select are enough to observe the strain rate sensitivity of the

Fig. 4. The components of the Instron 5567 Universal Test Machine used in our experiments: 1 is the main system; 2 is the supporting work station; 3 is the bespoke temperature chamber; 4 is a force sensor (±500 N); 5 is the crosshead.

polymer. Upon the increase of the strain rates, the stresses during the loading process become higher. The molecular chain movements may

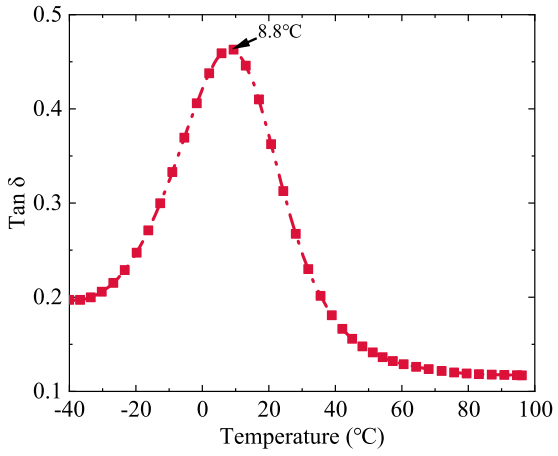

Fig. 5. Results of $\tan\delta$ obtained from DMA experiments to reveal the T_g value. Temperature-sensitivity phenomena of $\tan\delta$ can be seen.

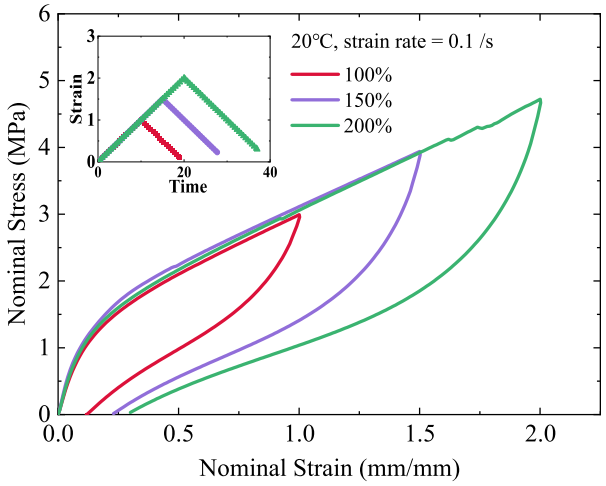

Fig. 6. Stress–strain curves of loading–unloading tests at 100%, 150%, and 200% strains under 20 °C. The inset depicts the strain controlling paths over time on the normal axis.

become stiffer upon the increase in strain rate, and the complicated entanglement network is likely to directly provide greater stress. In addition, at low strain rate, entanglements possibly have more time to unwind, which facilitates the deformation propagation, in other words, a lower stress response. It is also worth noting that the unloading paths under different strain rates are close to the same path, which suggests the strain rate independence for the unloading process.

From Figs. 6 and 7, the stress is found to be sensitive to the loading conditions, e.g., maximum strain level and strain rate, which are the typical responses of viscoelastic polymeric materials. The dissipation energy densities (the area enclosed by the loading and unloading curves) are depicted against the nominal strain and the strain rate, as shown in Figs. 8 and 9, respectively, to present the sensitivity of hysteresis phenomena.

3.3. Effects of temperature

To explore the temperature effect around the glass transition of EPU, several tests are carried out under different temperatures and the results are depicted in Fig. 10. Note that the illustration depicts the strain controlling paths over time on the normal axis. According to the curves, huge hysteresis and residual strains are observed, especially for the low-temperature cases, e.g., −20 °C. In addition, the Glass Transition, which

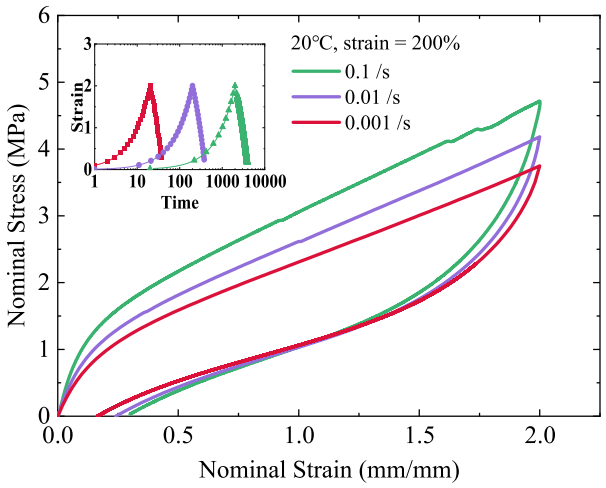

Fig. 7. Stress–strain curves of loading–unloading tests at 0.1 /s, 0.01 /s, and 0.001 /s strain rates at 20 °C. The inset depicts the strain controlling paths over time on the logarithmic axis.

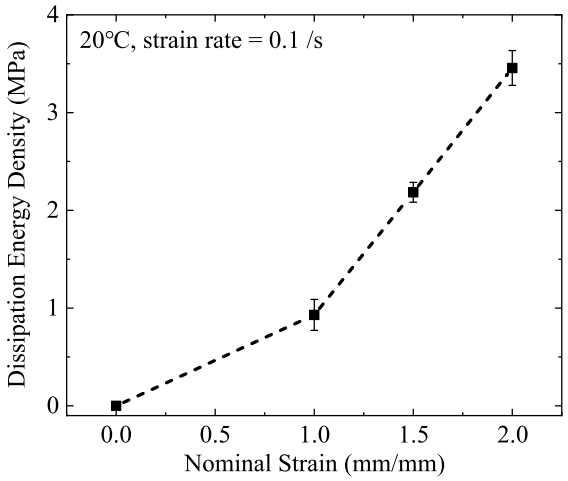

Fig. 8. Evolutions of the dissipation energy density with regard to strain on the normal axis.

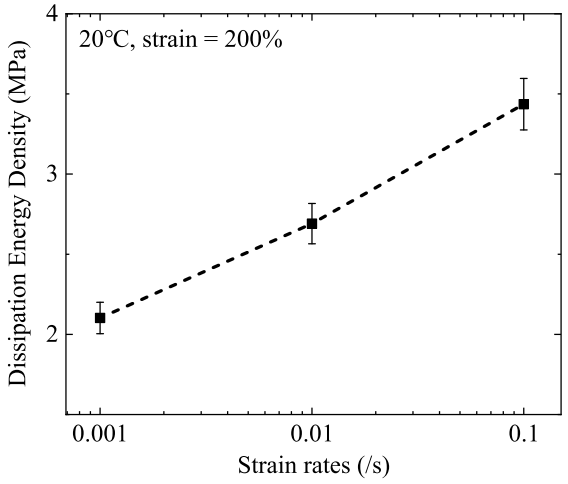

Fig. 9. Evolutions of the dissipation energy density with regard to strain rate on the logarithmic axis.

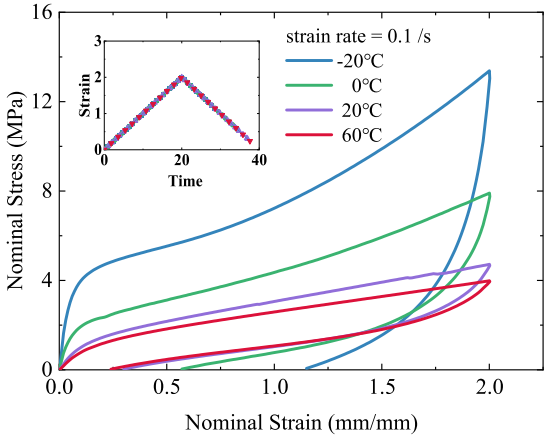

Fig. 10. Stress–strain curves of loading–unloading tests under −20 °C, 0 °C, 20 °C, and 60 °C. An obvious glass transition can be observed upon the decrease of temperature. The illustration depicts the strain controlling paths over time on the normal axis.

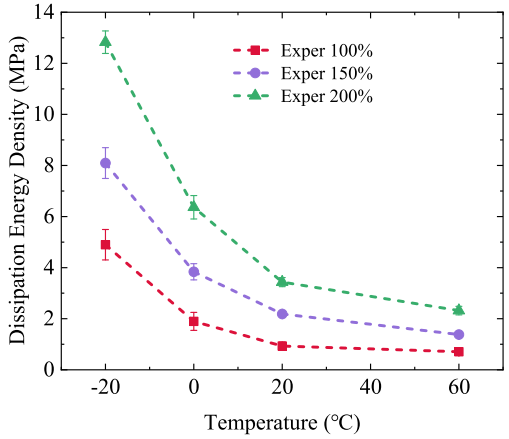

Fig. 11. Dissipation energy density versus temperature at different maximum strain levels. The phenomenon of large energy hysteresis is obvious at low temperatures.

is a significant change in the mechanical performance (e.g., Young's modulus), can be found under low-temperature conditions. The stress variations resulting from the temperature change are mainly due to viscosity variations. Specifically speaking, at low temperatures, chain segments are difficult to unwind, which hinders the deformation propagation and causes a high local stress response. The dissipation energy densities (MPa) under different temperatures and different maximum strain levels during loading–unloading experiments are depicted in Figs. 11 and 12 where the density decreases with the increase of temperature values and/or the decrease of maximum strain levels. The density decrements along temperature are more pronounced for the cases of lower temperatures for all three kinds of strain situations, which highlights the phenomenon of large energy hysteresis at low temperatures.

Fig. 13 depicts stress vs. time relationships during the loading–unloading experiments. The graph can be divided into two parts, i.e., the loading portion (0~20 s) and the unloading portion (20~36 s). As is shown, the lower the temperature, the higher the stress rises during the loading process. For instance, at −20 °C, the stress peaks at 13.4 MPa which is 2.8 times higher than that of 20 °C. However, for low-temperature cases, stress drops more quickly throughout the unloading process than in the high-temperature cases, resulting in larger residual strains (see Fig. 10). To more easily compare the trends of stress curves under high and low temperature conditions, a concept

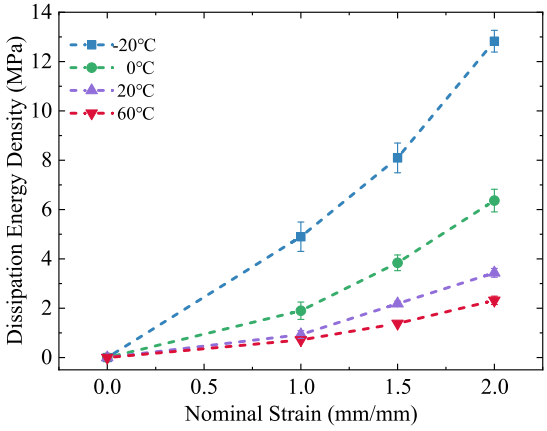

Fig. 12. Dissipation energy density versus nominal strain at different temperatures. The phenomenon of large energy hysteresis is obvious at large deformation.

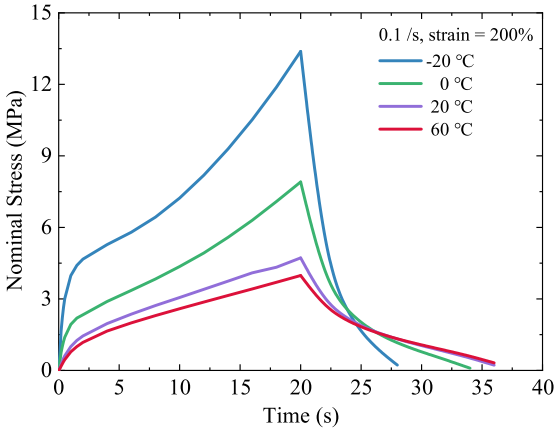

Fig. 13. The evolution trend of nominal stress with the change of time. The diagram can be divided into two parts, i.e., the loading portion (0~20 s) and the unloading portion (20~36 s).

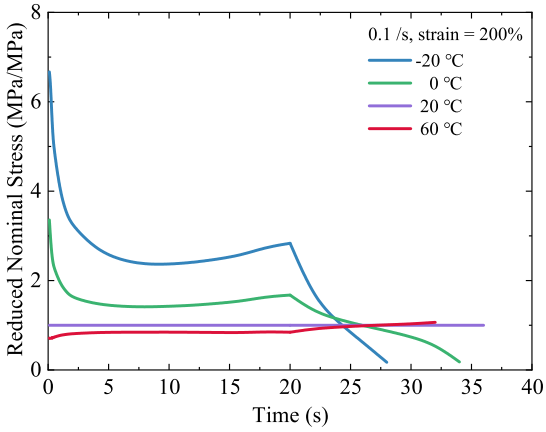

Fig. 14. The evolution trend of reduced nominal stress P_r with the change of time. The diagram can also be divided into two parts like Fig. 13.

of "Reduced Nominal Stress" (MPa/MPa), i.e.,

$$P_r = \frac{P_\Theta}{P_{\Theta_0}} \tag{1}$$

Table 3
Scaling parameters at −20 °C, 0 °C, 20 °C, and 60 °C.

Temperature [°C]	p_1	p_2	p_3	p_4
−20	2.49800	−0.28890	1.73300	0.02463
0	0.77440	−0.23560	1.07900	0.02201
20	1.00000	0.00000	0.00000	0.00000
60	0.86140	−0.00187	−0.12860	−0.51190

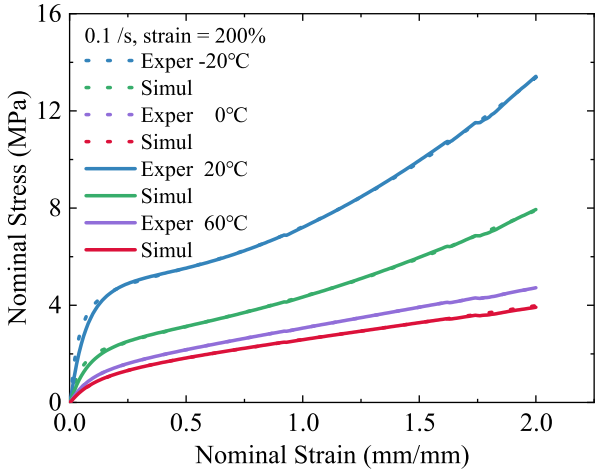

Fig. 15. The stress–strain relationships of the loading part in Fig. 10 and the simulated results by using Eq. (2).

is proposed here in which the reference temperature Θ_0 is chosen to be 20 °C. Therefore, when the temperature is 20 °C, $P_r = 1$ throughout the loading duration. Fig. 14 depicts the evolution trend of P_r with the change of time. Here, the data corresponding to 0.1 s is selected as the first point. During the loading portion, P_r decreases first and then grows at −20 °C and 0 °C, whereas an approximate constant (lower than the figure for 20 °C) can be seen at 60 °C except for a slightly increasing trend from 0 to around 2 s (i.e., 0.2 strain). This suggests that the temperature is not a mere linear factor during the stretching process (in particular, the initial stage), and the extents of influence from the temperature on either side of T_g are different. This may be because different temperatures affect the movements of segments and molecular chains differently (Yang et al., 2022). As for the unloading process, a proportional variation trend of P_r can be observed for all temperature conditions (see Fig. 14).

From the results of Figs. 13 and 14, EPU displays glassy state at the temperature ⩽20 °C and rubbery state at the temperature ⩾20 °C. In addition, the temperature dependence of stress at different strain levels is different as mentioned before. Therefore, a quantitative understanding on such temperature dependence is needed in order to inspire the constitutive modelling. After exploration, an exponential scaling strategy in the following form is found to well reproduce the loading experiments under different temperatures in Fig. 10:

$$P_\Theta = \left[p_1 \exp\left(p_2\varepsilon\right) + p_3 \exp\left(p_4\varepsilon\right)\right] P_{\Theta_0}, \tag{2}$$

where P_Θ and ε are the nominal stress and nominal strain, respectively. The experimental stress–strain relationship under the reference temperature Θ_0 (20 °C) and the reference strain rate (0.1 /s) is selected as P_{Θ_0}. P_Θ is obtained by multiplying the reference curve with the scaling function adjusted by parameters p_1, p_2, p_3, and p_4. All the scaling parameters are listed in Table 3, and the obtained curves are presented in Fig. 15. The reproducibility of the experimental results proves the reasonable use of the scaling strategy in exponential form to describe the temperature dependence.

All in all, the temperature effect can be simply summarised as follows:

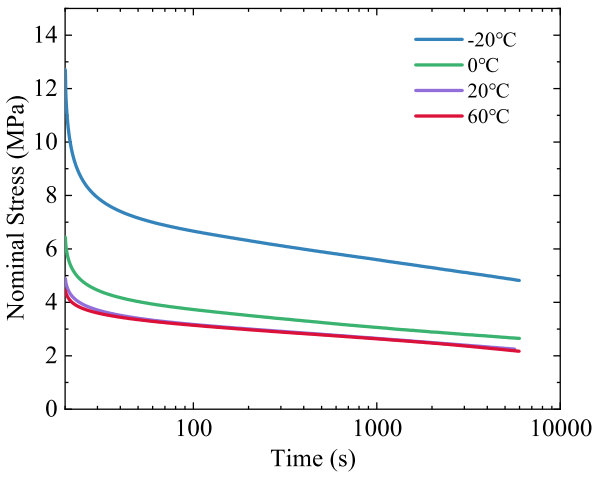

Fig. 16. Singe-step relaxation tests under different temperatures. Note that the loading curves are omitted here.

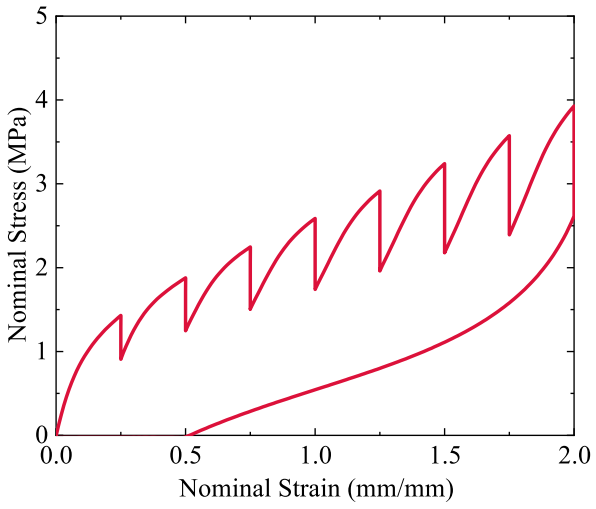

Fig. 17. Multi-step relaxation test under 20 °C at 25%, 50%, 75%, 100%, 125%, 150%, 175%, 200% strains.

- For the loading process, P_r varies linearly and highly nonlinearly with temperature in the rubbery state and glassy state, respectively.
- For the unloading process, proportional variation trends of the P_r can be observed for all temperature conditions.
- Temperature dependence is found to correlate with strain levels.
- A quantitative understanding on such temperature dependence inspires us to use a temperature-strain coupled scaling strategy in the constitutive modelling.

3.4. Stress relaxation tests

The total stress response of a soft polymer is considered as a combination of non-equilibrium and equilibrium stresses, which is a typical manifestation of viscoelastic behaviour (Nikoukalam and Sideris, 2019; Liao et al., 2019; Hossain et al., 2020; Hossain and Liao, 2020; Liao et al., 2020b). Note that the non-equilibrium stress is rate- and temperature-dependent as mentioned above. As for the equilibrium stress, the single-step relaxation test is an effective method to investigate the temperature influence.

Fig. 16 shows the results of single-step relaxation experiments under −20 °C, 0 °C, 20 °C, and 60 °C. Each test is held at 200% strain

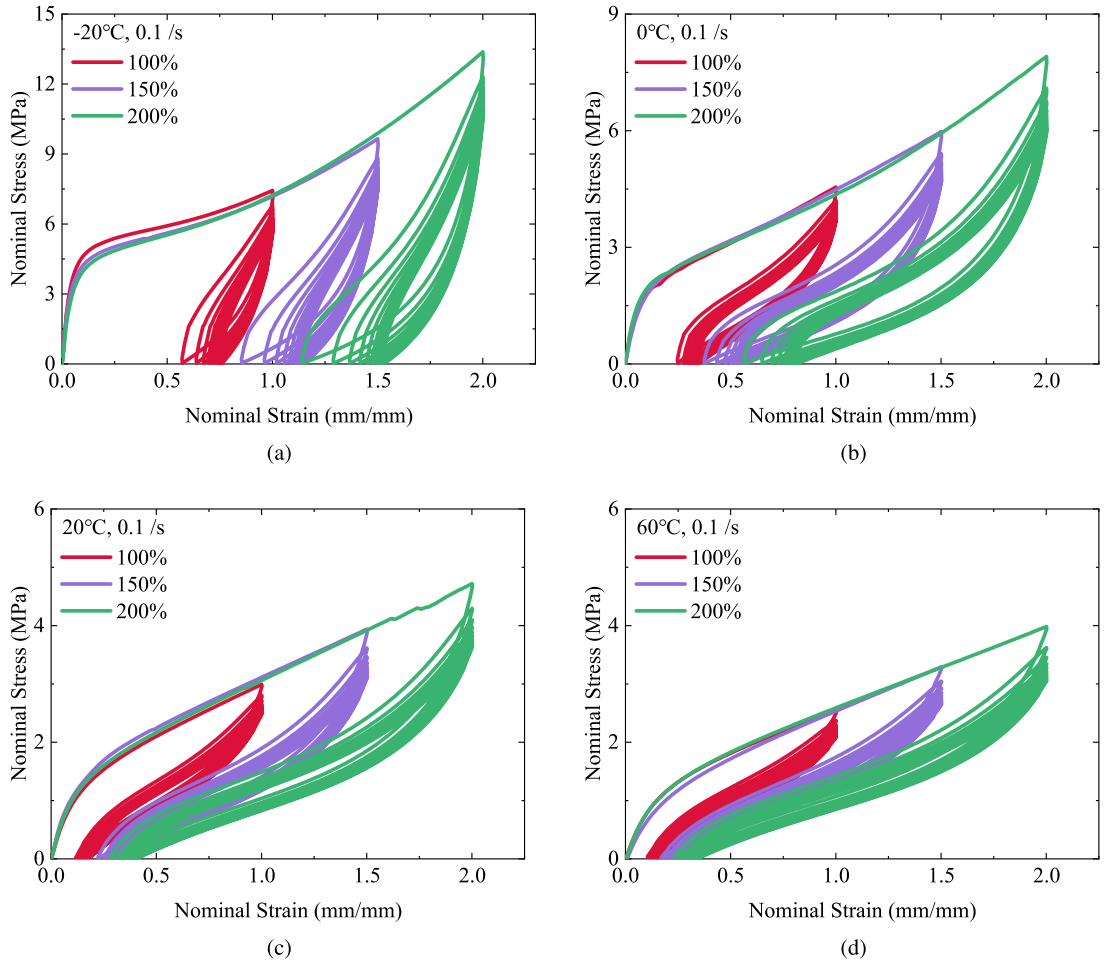

Fig. 18. Stress strain relationships in loading–unloading cyclic experiments under (a) −20 °C, (b) 0 °C, (c) 20 °C, and (d) 60 °C. Each curve shows three different strain levels, i.e., 100%, 150%, and 200%. In these four curves, the relationships between stress and hysteretic energy with loading times, temperature, and strain levels are well depicted.

for 6000 s. Note that the time is displayed on the logarithmic axis and the loading part is omitted here. As shown in Fig. 16, each line decreases quickly within the first few seconds, especially for the low-temperature cases, and then gradually levels off to a non-zero value. According to our previous studies (Hossain and Liao, 2020; Liao et al., 2020b), this stable value is termed the equilibrium stress, which does not change significantly further with time. The figure for −20 °C is larger than the other three cases at the relaxation time of 6000 s due to the huge viscosity at this low temperature, while the other three ones have a clear trend to approach the same value. From the trend of the curves in Fig. 16, we find their slopes are different. At a higher temperature level, the relaxation curve shows a faster-decreasing trend. Therefore, we may probably assume that curves will eventually level off to the same value for different temperatures for an infinite period of relaxation, which suggests the possible temperature independence of the equilibrium stress. Note that this is only an assumption, and it may not be true, as it is not practical to verify. Similar phenomena and assumptions have also been seen in previous studies (Hossain and Liao, 2020).

Based on our definition of the equilibrium stress, for a certain material, the equilibrium path is the same regardless of the test modes. Therefore, we also display the result of multi-step relaxation experiments at 25%, 50%, 75%, 100%, 125%, 150%, 175%, 200% strains, as seen in Fig. 17. The experiments are carried out under 20 °C, and are held every 25% strain internal for 3600 s. By recording the stress levels at the endpoint of each strain internal, the equilibrium stresses can also be extracted.

3.5. Cyclic loading–unloading tests

The thermo-mechanical properties of EPU are explored further by cyclic loading–unloading experiments, as shown in Fig. 18 under different temperatures and maximum strain levels. The subsequent loading curves are always lower than the previous loading curves at each condition, which is a typical property of the viscosity of EPU (Dorfmann and Ogden, 2004; Dorfmann et al., 2007; Qi and Boyce, 2005b). The loading curves become closer and closer with the increase in loading times. The same trend is observed for the unloading curves. The evolution trends of peak stresses, residual strains, and dissipation energy densities with cyclic loading times are shown in Fig. 19 for −20 °C, 0 °C, 20 °C, and 60 °C, respectively. The reductions of dissipation energy densities for all the temperature cases are mainly taking place before the second loading cycle. Upon the increase in loading times, the convergence of these three values can be seen. However, the hysteresis phenomenon persists regardless of the loading times. Note that in our previous work on the silicone rubbers, it was found that the reloading path overlaps the unloading path after some loading times (Yousaf et al., 2020; Liao et al., 2021). This is probably because the hysteresis properties differ among soft polymers, which have diverse and complicated chain entanglement networks.

4. Constitutive modelling

In this section, a phenomenologically-motivated thermo-viscoelastic constitutive model is developed based on continuum mechanics and following relevant laws of thermo-dynamics at finite deformations (Holzapfel, 2000; Reese and Govindjee, 1998).

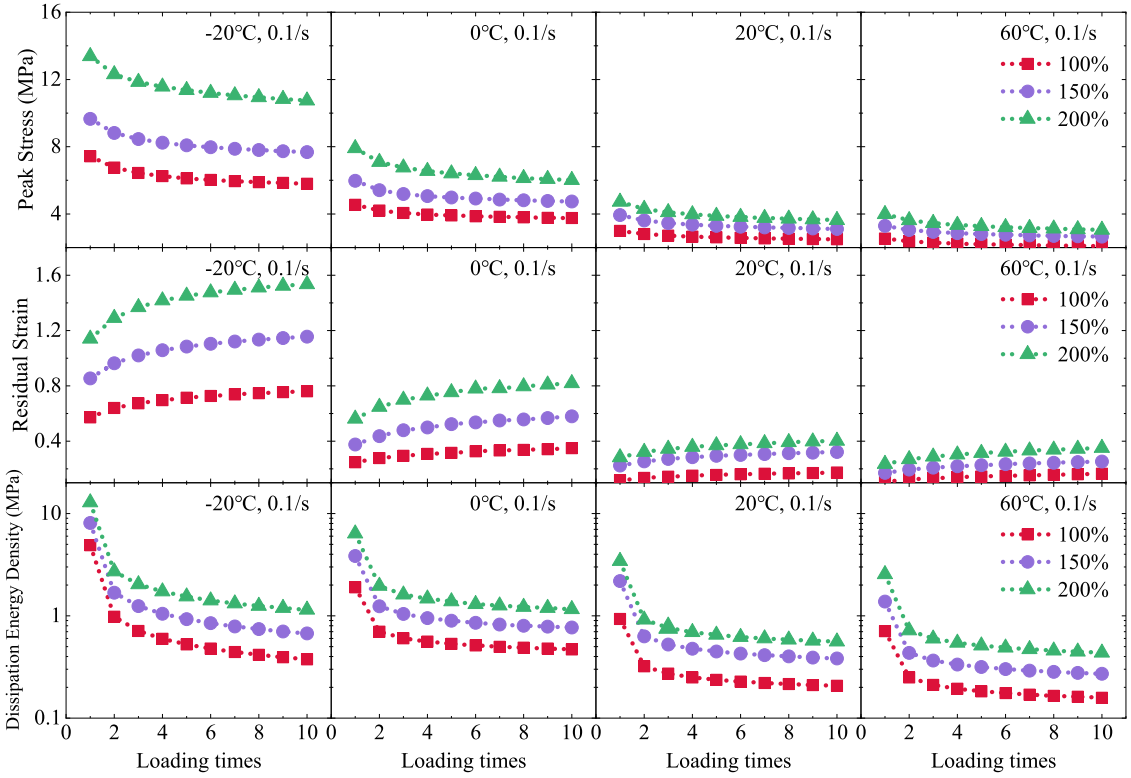

Fig. 19. The evolution of peak stress, residual strain, and dissipation energy density with cyclic loading under −20 °C, 0 °C, 20 °C, and 60 °C. The three lines in each subfigure represent different strain levels, i.e., 100%, 150%, and 200%.

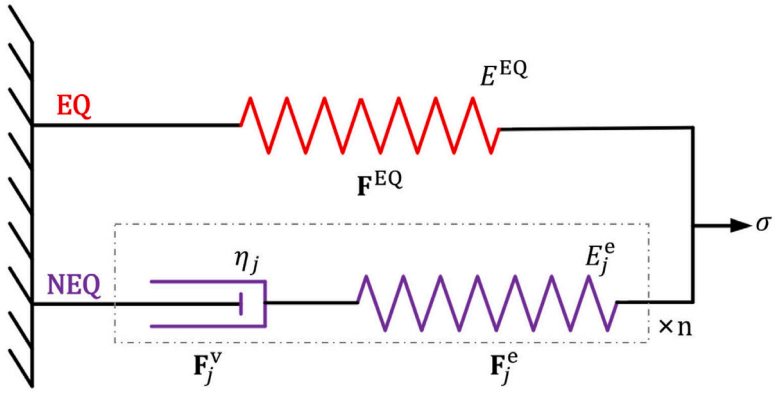

Fig. 20. The rheological model for viscoelastic material behaviour. Note that $\mathbf{F}^{EQ}$ denotes the deformation gradient of EQ branch, and $\mathbf{F}_j^v$ and $\mathbf{F}_j^e$ are the viscous part and the elastic part of deformation gradient of the jth of n parallel Maxwell elements. In addition, E^{EQ}, η_j, and E_j^e represent the spring constant of EQ branch, the viscosity and spring constant of the jth NEQ branch, respectively.

4.1. Kinematics

Considering the influence of mechanical motion (e.g., stretching) and temperature variation (e.g., thermal expansion) to the deformation, the deformation gradient tensor **F** can be multiplicatively decomposed into two parts as (Lion, 1997; Lu and Pister, 1975; Reese and Govindjee, 1997; Liao et al., 2020b)

$$\mathbf{F} = \mathbf{F}_{\mathrm{M}}\mathbf{F}_{\Theta}, \tag{3}$$

where M and Θ denote the abbreviated forms of "the mechanical deformation" and "the absolute temperature", respectively.

To process further, a rheology model (schematically shown in Fig. 20), which has an equilibrium (EQ) branch and n non-equilibrium (NEQ) branches, are considered. The total stress of this model is the sum of the stresses in each branch (Xiang et al., 2020; Liao et al., 2020b,a; Hossain and Liao, 2020) and the deformation is identical for every branch all the time (Xiang et al., 2020). To capture the time-dependent viscoelastic response at finite strains, a multiplicative decomposition of the deformation gradient is frequently used which yields further as

$$\mathbf{F} = \mathbf{F}_{\mathrm{M}}\mathbf{F}_{\Theta} = \mathbf{F}_{\mathrm{M}}^{\mathrm{vol}}\mathbf{F}_{\mathrm{M}}^{\mathrm{iso}}\mathbf{F}_{\Theta} = \mathbf{F}_{\mathrm{M}}^{\mathrm{vol}}\mathbf{F}_{\mathrm{M},j}^{\mathrm{e}}\mathbf{F}_{\mathrm{M},j}^{\mathrm{v}}\mathbf{F}_{\Theta} \quad (j = 1, \ldots, n), \tag{4}$$

where $j = 1, \ldots, n$ is related to the possibility of multiple viscous mechanisms with each one represented by a Maxwell element. Note that according to some previous studies (Reese and Govindjee, 1997; Dippel et al., 2015), $\mathbf{F}^{\mathrm{e}}_{\mathrm{M},j}$ and $\mathbf{F}^{\mathrm{v}}_{\mathrm{M},j}$ are assumed to be isochoric only. Furthermore, we can use the deformation gradient $\mathbf{F}$ for the definition of the right Cauchy–Green tensor $\mathbf{C} = \mathbf{F}^{\mathrm{T}}\mathbf{F}$. The corresponding elastic and inelastic right Cauchy–Green strain tensors are defined as $\mathbf{C}^{\mathrm{e}}_{\mathrm{M},j} = [\mathbf{F}^{\mathrm{e}}_{\mathrm{M},j}]^{\mathrm{T}}\mathbf{F}^{\mathrm{e}}_{\mathrm{M},j}$ and $\mathbf{C}^{\mathrm{v}}_{\mathrm{M},j} = [\mathbf{F}^{\mathrm{v}}_{\mathrm{M},j}]^{\mathrm{T}}\mathbf{F}^{\mathrm{v}}_{\mathrm{M},j}$, respectively. We here introduce the thermal expansion coefficient α and the temperature difference ($\Delta\Theta = \Theta - \Theta_0$) which results in the decomposition of the Jacobian determinant into

$$J = \det \mathbf{F} = \det \mathbf{F}_{\mathrm{M}} \ \det \mathbf{F}_{\Theta} = J_{\mathrm{M}} J_{\Theta}, \tag{5}$$

where the thermal Jacobian is scaled either with an exponential function as $J_{\Theta} = \exp(3\alpha\Delta\Theta)$ or with a linear function, i.e., $J_{\Theta} = \alpha\Delta\Theta + 1$. Finally, as rubber-like materials can be assumed to be incompressible at a constant temperature, the decomposition between the mechanical and the thermal deformation resembles a decomposition into a purely isochoric and a purely volumetric deformation. In this case, we can state that

$$J_{\mathrm{M}} = 1 \quad \text{and} \quad J = J_{\Theta}. \tag{6}$$

4.2. A thermo-viscoelastic energy function

According to Liao et al. (2020b), Hossain and Liao (2020) and Mehnert et al. (2021), a strain energy function Ψ can be used to describe the thermo-mechanical behaviour of EPU:

$$\Psi = \Psi(\mathbf{C}, \mathbf{X}_1, \ldots, \mathbf{X}_n, \Theta), \tag{7}$$

where $\mathbf{X}_j$ ($j = 1, \ldots, n$) denote the internal variables. To determine the internal variable $\mathbf{X}_j$, a series of evolution functions

$$\dot{\mathbf{X}}_j = \mathcal{Z}(\mathbf{C}, \mathbf{X}_1, \ldots, \mathbf{X}_n) \tag{8}$$

are needed. Inspired by Reese and Govindjee (1997), the elastic deformation associated with the spring in the jth Maxwell element

$$\mathbf{C}^{\mathrm{e}}_{\mathrm{M},j} = \left[\mathbf{F}^{\mathrm{e}}_{\mathrm{M},j}\right]^{\mathrm{T}} \mathbf{F}^{\mathrm{e}}_{\mathrm{M},j} = \left[\mathbf{F}^{\mathrm{v}}_{\mathrm{M},j}\right]^{-\mathrm{T}} \cdot \mathbf{C}_{\mathrm{M}} \cdot \left[\mathbf{F}^{\mathrm{v}}_{\mathrm{M},j}\right]^{-1} \tag{9}$$

is selected as the internal variable $\mathbf{X}_j$. Therefore, for an isotropic nearly incompressible soft material, a reasonable hypothesis for the temperature-dependent free energy function can be described as

$$\begin{aligned} \Psi &= \underbrace{\Psi_{\mathrm{M,vol}} + \Psi^{\mathrm{EQ}}_{\mathrm{M,iso}} + \Psi^{\mathrm{NEQ}}_{\mathrm{M,iso}}}_{\text{Mechanical part}} + \underbrace{\Psi_{\Theta}}_{\text{Thermal part}} \\ &= \Psi^{\mathrm{EQ}}_{\mathrm{M,iso}}(\mathbf{C}_{\mathrm{M}}, \Theta) + \Psi^{\mathrm{NEQ}}_{\mathrm{M,iso}}(\mathbf{C}^{\mathrm{e}}_{\mathrm{M},1}, \ldots, \mathbf{C}^{\mathrm{e}}_{\mathrm{M},n}, \Theta) + \Psi_{\Theta}, \end{aligned} \tag{10}$$

where

$$\mathbf{C}_{\mathrm{M}} = \mathbf{F}^{\mathrm{T}}_{\mathrm{M}}\mathbf{F}_{\mathrm{M}}. \tag{11}$$

Note that we neglect $\Psi_{\mathrm{M,vol}}$ as it is assumed that $J_{\mathrm{M}} = 1$. In addition, we assume the independence of internal variables for $\Psi^{\mathrm{EQ}}_{\mathrm{M,iso}}$, and for the last term Ψ_{Θ}, it can be divided into two parts (Hossain and Liao, 2020; Liao et al., 2020b):

$$\Psi_{\Theta} = -\left[\Theta - \Theta_0\right] M(J_{\Theta}) - c_0 \left[\Theta - \Theta_0 - \Theta \ln\left(\frac{\Theta}{\Theta_0}\right)\right], \tag{12}$$

where Θ_0 is the reference temperature, $M(J_{\Theta})$ states the purely volumetric thermal expansion, c_0 is a constant related to the specific heat capacity. Eq. (12) represents the energy composition arising from the thermal expansion and the variation of heat capacity. Note that since in this study, the influence of temperature is measured only on the stress response and we do not have data on the thermal expansion (or contraction), the thermal decomposition of the deformation is simplified henceforth. It effectively equates the total deformation gradient to its mechanical part only, i.e., $\mathbf{F} = \mathbf{F}_{\mathrm{M}}\mathbf{F}_{\Theta} = \mathbf{F}_{\mathrm{M}}$ and $\mathbf{C} = \mathbf{C}_{\mathrm{M}}$.

4.3. Three-dimensional constitutive model for thermo-viscoelastic behaviours

The constitutive equation is further required to fulfil the second law of thermodynamics in the form of the Clausius–Duhem inequality (Reese and Govindjee, 1997):

$$\frac{1}{2}\mathbf{S} : \dot{\mathbf{C}} + p\mathbf{C}^{-1} : \frac{1}{2}\dot{\mathbf{C}} - \dot{\Psi} - \xi\dot{\Theta} - \frac{\mathbf{Q}}{\Theta} \cdot \mathrm{Grad}\Theta \geq 0, \tag{13}$$

where $\mathbf{S}$ is the temperature-dependent expression of the second Piola–Kirchhoff stress, p is a scalar Lagrange multiplier accounting for the indeterminate pressure because of the incompressibility of rubber-like polymers (Liao et al., 2020a), ξ represents the entropy per unit reference volume, and $\mathbf{Q} = J\mathbf{F}^{-1} \cdot \mathbf{q}$, where $\mathbf{q}$ is the spatial heat flux vector. Combined Eqs. (7) and (13), the more detailed entropy inequality can be written as:

$$\left[\mathbf{S} + p\mathbf{C}^{-1} - 2\frac{\partial\Psi}{\partial\mathbf{C}}\right] : \frac{1}{2}\dot{\mathbf{C}} - \left[\frac{\partial\Psi}{\partial\Theta} + \xi\right]\dot{\Theta} - \sum_{j=1}^{n} \frac{\partial\Psi}{\partial\mathbf{X}_j} : \dot{\mathbf{X}}_j - \frac{\mathbf{Q}}{\Theta} \cdot \mathrm{Grad}\Theta \geq 0. \tag{14}$$

In terms of thermodynamics, Eq. (14) should be satisfied throughout the deformation for a continuous system. Therefore, considering Eq. (10) and the arbitrary values of $\dot{\mathbf{C}}$ and $\dot{\Theta}$ in Eq. (14), $\mathbf{S}$ and ξ can be described as

$$\mathbf{S} = -p\mathbf{C}^{-1} + 2\frac{\partial\Psi}{\partial\mathbf{C}} \tag{15}$$

$$\xi = -\frac{\partial\Psi}{\partial\Theta}, \tag{16}$$

where p should be determined by appropriate boundary conditions. It is worth noting that we do not consider Ψ_{Θ} in Eq. (15) since it is assumed to be independent with $\mathbf{C}$ and time (Eq. (12)). By utilising Eqs. (10), (15), and Eq. (16) in Eq. (14), the residual inequality gives

$$-\sum_{j=1}^{n} \frac{\partial\Psi^{\mathrm{NEQ}}_{\mathrm{iso}}}{\partial\mathbf{C}^{\mathrm{e}}_{j}} : \dot{\mathbf{C}}^{\mathrm{e}}_{j} - \frac{\mathbf{Q}}{\Theta} \cdot \mathrm{Grad}\Theta \geq 0, \tag{17}$$

which indicates the non-negativity of internal energy consumption. In the experimental section, only mechanical stresses are calculated and any temperature-dependent stress is discarded. Thus, combining Eqs. (10) and (15),

$$\mathbf{S} = -p\mathbf{C}^{-1} + 2\frac{\partial\Psi^{\mathrm{EQ}}_{\mathrm{iso}}(\mathbf{C}, \Theta)}{\partial\mathbf{C}} + 2\frac{\partial\Psi^{\mathrm{NEQ}}_{\mathrm{iso}}(\mathbf{C}^{\mathrm{e}}_{1}, \ldots, \mathbf{C}^{\mathrm{e}}_{n}, \Theta)}{\partial\mathbf{C}}. \tag{18}$$

Finally the equilibrium (mechanical) stress (hyperelastic stress) $\mathbf{S}^{\mathrm{EQ}}$ and the non-equilibrium stress (viscoelastic stress) $\mathbf{S}^{\mathrm{NEQ}}$ result in

$$\mathbf{S}^{\mathrm{EQ}} = 2\frac{\partial\Psi^{\mathrm{EQ}}_{\mathrm{iso}}}{\partial\mathbf{C}}, \tag{19}$$

$$\mathbf{S}^{\mathrm{NEQ}} = 2\frac{\partial\Psi^{\mathrm{NEQ}}_{\mathrm{iso}}}{\partial\mathbf{C}}, \tag{20}$$

respectively.

In order to simplify the constitutive model, $\Psi^{\mathrm{EQ}}_{\mathrm{iso}}$ and $\Psi^{\mathrm{NEQ}}_{\mathrm{iso}}$ are assumed to be influenced merely by the strain invariants. Due to the highly non-linear response of EPU, the Carroll model is chosen as the equilibrium strain energy function (Hossain and Liao, 2020),

$$\Psi^{\mathrm{EQ}}_{\mathrm{iso}} = \left[\frac{\Theta}{\Theta_0} + g^{\mathrm{e}}\right]\left[aI_1 + bI_1^4 + c\sqrt{I_2}\right], \tag{21}$$

where g^{e} is a temperature scaling function, I_1 and I_2 are the first and second strain invariants, respectively, of $\mathbf{C}$, and a, b, c are material constants. Here, for simplification, we do not consider the temperature-dependence of $\Psi^{\mathrm{EQ}}_{\mathrm{iso}}$ in this contribution, which gives $g^{\mathrm{e}} = 1 - \frac{\Theta}{\Theta_0}$. By substituting Eq. (21) into Eq. (19), the corresponding equilibrium stress can be expressed as

$$\mathbf{S}^{\mathrm{EQ}} = \left[2a + 8bI_1^3\right]\mathbf{I} + c\left[I_1\mathbf{I} - \mathbf{C}\right] I_2^{-\frac{1}{2}} \tag{22}$$

where $\mathbf{I}$ is a second order identity tensor. In terms of the non-equilibrium response, a viscous energy function is chosen as

$$\Psi_{\text{iso}}^{\text{NEQ}} = \left[\frac{\Theta}{\Theta_0} + g^{\text{v}}\right]\left[d\left[\left[I_{1,1}^{\text{e}}\right]^3 - 3^3\right] + eI_1^2\left[I_{1,2}^{\text{e}} - 3\right]\right], \tag{23}$$

where g^{v} is also a temperature scaling function like g^{e}, $I_{1,j}^{\text{e}}$ $(j = 1, 2)$ is the first strain invariant of $\mathbf{C}_j^{\text{e}}$, and d, e are material constants. Here, g^{v} is considered to be correlated with temperature and mechanical deformation simultaneously, i.e., $g^{\text{v}} = g(\mathbf{C}, \Theta)$. By substituting Eq. (23) into Eq. (20), the non-equilibrium stress is described as

$$\begin{aligned}\mathbf{S}^{\text{NEQ}} = {} & 2\left[\frac{\partial g^{\text{v}}}{\partial \mathbf{C}}\right]\left[d\left[\left[I_{1,1}^{\text{e}}\right]^3 - 3^3\right] + eI_1^2\left[I_{1,2}^{\text{e}} - 3\right]\right] \\ & + \left[\frac{\Theta}{\Theta_0} + g^{\text{v}}\right]\left[6d\left[I_{1,1}^{\text{e}}\right]^2\left[\mathbf{C}_1^{\text{v}}\right]^{-1} + 2e\left[I_1\right]^2\left[\mathbf{C}_2^{\text{v}}\right]^{-1}\right. \\ & \left. + 4eI_1\left[I_{1,2}^{\text{e}} - 3\right]\mathbf{I}\right].\end{aligned} \tag{24}$$

Now, a series of evolution equations are required to track the time-dependent response of the internal variables. According to the works of Reese and Govindjee (1998), Scheffer et al. (2015), and Hossain and Liao (2020), a classical finite strain linear evolution function can be given as

$$\dot{\overline{\mathbf{C}_j^{\text{v}}}} = \frac{1}{\tau_j}\left[\mathbf{C} - \mathbf{C}_j^{\text{v}}\right], \tag{25}$$

where τ_j is the relaxation time related to the current deformation and deformation rate (Scheffer et al., 2015; Koprowski-Theiss et al., 2011). It can be described as

$$\tau_j = \tau_{j1} + \tau_{j2}\exp\left(-k_j\|\mathbf{D}\|\sqrt{\|\mathbf{C}\|}\right), \tag{26}$$

where

$$\mathbf{D} = \frac{1}{2}(\mathbf{L} + \mathbf{L}^{\text{T}}); \quad \mathbf{L} = \dot{\mathbf{F}}\cdot\mathbf{F}^{-1}. \tag{27}$$

Here, $\mathbf{D}$ is the rate of deformation tensor, $\mathbf{L}$ is the derivative of the velocity gradient, and $\|\bullet\|$ stands for the norm of $\bullet$. Note that, as illustratively explained by Reese and Govindjee (1998), this (Eq. (25)) linear finite strain evolution equation is restricted to states close to the thermodynamical equilibrium.

4.4. Uniaxial reduction

When it comes to parameter identification and model validation with experimental data, a good way is to decouple the complex three-dimensional constitutive models into a set of one-dimensional equations. When uniaxial tension experiments are considered and following the incompressibility condition, $\mathbf{F}$ and $\mathbf{C}$ can be written as

$$\mathbf{F} = \begin{bmatrix} \lambda & 0 & 0 \\ 0 & \lambda^{-1/2} & 0 \\ 0 & 0 & \lambda^{-1/2} \end{bmatrix}, \tag{28}$$

$$\mathbf{C} = \begin{bmatrix} \lambda^2 & 0 & 0 \\ 0 & \lambda^{-1} & 0 \\ 0 & 0 & \lambda^{-1} \end{bmatrix}, \tag{29}$$

where λ is the elongation in the uniaxial tension direction. The strain invariants can be written as

$$I_1 = \frac{2}{\lambda} + \lambda^2; \quad I_2 = 2\lambda + \frac{1}{\lambda^2}; \quad I_3 = 1. \tag{30}$$

Following the relevant relationship between the first Piola–Kirchhoff stress and the second Piola–Kirchhoff stress, i.e., $\mathbf{P} = \mathbf{FS}$, the equilibrium axial stress for the uniaxial case can be written as

$$\text{P}^{\text{EQ}} = \left[2a + 8b[\frac{2}{\lambda} + \lambda^2]^3 + 2c[1 + 2\lambda^3]^{-\frac{1}{2}}\right]\left[\lambda - \frac{1}{\lambda^2}\right]. \tag{31}$$

The non-equilibrium axial stress can be written as

$$\begin{aligned}\text{P}^{\text{NEQ}} = {} & 2\phi(\lambda,\Theta)\left[d\left[\left[\frac{2\lambda_1^{\text{v}}}{\lambda} + \frac{\lambda^2}{\left[\lambda_1^{\text{v}}\right]^2}\right]^3 - 3^3\right] + e\left[\frac{2}{\lambda} + \lambda^2\right]^2\right. \\ & \left.\times\left[\frac{2\lambda_2^{\text{v}}}{\lambda} + \frac{\lambda^2}{\left[\lambda_2^{\text{v}}\right]^2} - 3\right]\right] \\ & + \left[\frac{\Theta}{\Theta_0} + g^{\text{v}}\right]\left[6d\left[\frac{2\lambda_1^{\text{v}}}{\lambda} + \frac{\lambda^2}{\left[\lambda_1^{\text{v}}\right]^2}\right]^2\left[\frac{\lambda}{\left[\lambda_1^{\text{v}}\right]^2} - \frac{\lambda_1^{\text{v}}}{\lambda^2}\right]\right. \\ & + 2e\left[\frac{2}{\lambda} + \lambda^2\right]^2\left[\frac{\lambda}{\left[\lambda_2^{\text{v}}\right]^2} - \frac{\lambda_2^{\text{v}}}{\lambda^2}\right] \\ & \left. + 4e\left[\frac{2}{\lambda} + \lambda^2\right]\left[\frac{2\lambda_2^{\text{v}}}{\lambda} + \frac{\lambda^2}{\left[\lambda_2^{\text{v}}\right]^2} - 3\right]\left[\lambda - \frac{1}{\lambda^2}\right]\right],\end{aligned} \tag{32}$$

where

$$\phi(\lambda,\Theta) = \frac{\partial g^{\text{v}}}{\partial\left[\lambda^2\right]}\lambda - \frac{\partial g^{\text{v}}}{\partial\left[\frac{1}{\lambda}\right]}\frac{1}{\lambda^2} = \frac{3}{2}\frac{\partial g^{\text{v}}}{\partial\lambda}, \tag{33}$$

$$\lambda = \lambda_j^{\text{e}}\lambda_j^{\text{v}}. \tag{34}$$

The corresponding evolution functions of λ_j^{v} are

$$\dot{\overline{\left[\lambda_j^{\text{v}}\right]^2}} = \frac{1}{\tau_j}\left[\lambda^2 - \left[\lambda_j^{\text{v}}\right]^2\right], \quad j = 1, 2, \tag{35}$$

where

$$\tau_j = \tau_{j1} + \tau_{j2}\exp\left(-\sqrt{\frac{3}{2}}k_j\left|\dot{\lambda}\right|\sqrt[4]{1 + \frac{2}{\lambda^6}}\right). \tag{36}$$

In this contribution, we use the Euler-backward scheme to solve the differential equation (35). Note that the incompressibility has been considered in the expressions of Eqs. (31) and (32). So far, based on the second law of thermodynamics, a phenomenological thermo-viscoelastic constitutive model has been built based on non-linear continuum mechanics and thermodynamics. In the next section, the parameters identification process would be carried out using the experimental data described in Section 3.

4.5. Parameters identification

4.5.1. At the reference temperature Θ_0

In this section, the constitutive model under the reference temperature $\Theta_0 = 20$ °C is considered so that we can obtain the hyperelastic parameters and viscoelastic parameters first. Note that absolute temperature (K) is used for the parameter identification. At Θ_0, the term of $\left[\frac{\Theta}{\Theta_0} + g^{\text{v}}\right]$ in Eq. (23) equals to 1, and $\phi(\lambda, \Theta_0)$ is set to 0 (see Section 4.5.2). Therefore, the expression of Eq. (32) is simplified as

$$\begin{aligned}\text{P}^{\text{NEQ}} = {} & 6d\left[\frac{2\lambda_1^{\text{v}}}{\lambda} + \frac{\lambda^2}{\left[\lambda_1^{\text{v}}\right]^2}\right]^2\left[\frac{\lambda}{\left[\lambda_1^{\text{v}}\right]^2} - \frac{\lambda_1^{\text{v}}}{\lambda^2}\right] \\ & + 2e\left[\frac{2}{\lambda} + \lambda^2\right]^2\left[\frac{\lambda}{\left[\lambda_2^{\text{v}}\right]^2} - \frac{\lambda_2^{\text{v}}}{\lambda^2}\right] + 4e\left[\frac{2}{\lambda} + \lambda^2\right]\left[\frac{2\lambda_2^{\text{v}}}{\lambda} + \frac{\lambda^2}{\left[\lambda_2^{\text{v}}\right]^2} - 3\right] \\ & \times\left[\lambda - \frac{1}{\lambda^2}\right].\end{aligned} \tag{37}$$

For the parameter identification process, a Least Square Method built-in within `Matlab` is used. As seen in the experimental results in Figs. 13 and 14, temperature has different effects on the mechanical properties for different states of EPU. The reference strain rate is chosen as 0.1 /s. In addition, a Newton iteration algorithm is used to find the update of the internal variables appearing in the evolution functions. To determine the equilibrium composition of the total stress, the multi-step relaxation experimental data are used first which is a useful strategy

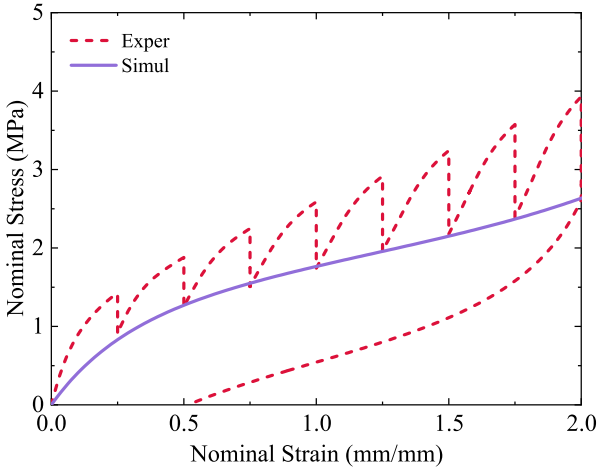

Fig. 21. Carroll model: multi-step relaxation experiment is carried out to extract the equilibrium path with 0.1 /s loading and 1 h relaxation at every 0.25 strain interval. The short dashed line is the experiment data, and the solid line is the simulated result.

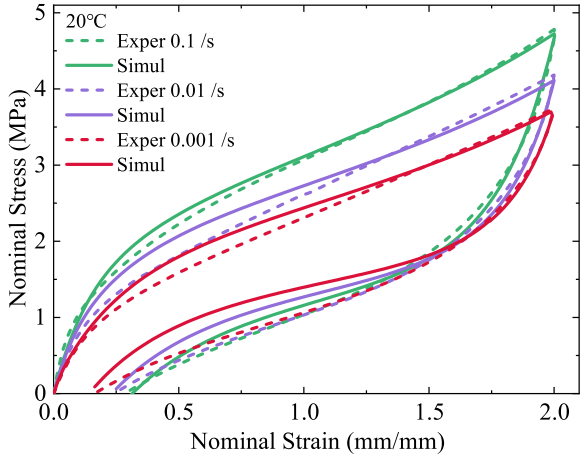

Fig. 22. Viscoelasticity model: general uniaxial tension experiments under 20 °C are carried out to obtain the viscoelastic parameters. The short dashed lines are the experiment data, and the solid lines are the simulated results.

Table 4
Hyperelastic parameters.

a [MPa]	b [MPa]	c [MPa]
0.285467	0.000015	0.871497

for separating the total stress into two portions: equilibrium stress and non-equilibrium stress (Nikoukalam and Sideris, 2019; Liao et al., 2019; Hossain et al., 2020). As shown in Fig. 21, the experimental equilibrium path is well-reproduced, implying that the Carroll model of Eq. (31) can well simulate the nonlinear equilibrium path under finite deformation. Furthermore, to identify the viscoelastic parameters, loading–unloading cyclic test data obtained at varying loading rates of 0.1 /s, 0.01 /s, and 0.001 /s are utilised simultaneously. The simulated results reproduce the experimental data well thanks to the reasonable expression of relaxation time τ_j, as depicted in Fig. 22. All hyperelasticity and viscoelastic parameters are specified in Tables 4 and 5. Good capability of the constitutive model to capture the experimental data can be seen.

4.5.2. Modelling the temperature effects

Inspired by the experimental findings in Section 3.3, we devise the exponential temperature scaling strategy to describe the influence of temperature on the curve trends, which proves the rationalisation of the modular g^{v}. Here, we give the expression of g^{v} in Eq. (23) as

$$g^{\mathrm{v}} = -\frac{\Theta}{\Theta_0} + g_{\mathrm{r}}^{\mathrm{v}} + g_{\mathrm{g}}^{\mathrm{v}}, \tag{38}$$

where the subscripts of "r" and "g" mean rubbery state and glassy state, respectively, and the forms of $g_{\mathrm{r}}^{\mathrm{v}}$ and $g_{\mathrm{g}}^{\mathrm{v}}$ are given as

$$g_{\mathrm{r}}^{\mathrm{v}} = \frac{1}{2}[\tanh(\Theta - T_{\mathrm{g}}) + 1]\left(\frac{\Theta_0}{\Theta}\right)^{n_1}, \tag{39}$$

$$g_{\mathrm{g}}^{\mathrm{v}} = \frac{n_3}{2}\left[-\tanh(\Theta - T_{\mathrm{g}}) + 1\right]\left[\left(\frac{\Theta_0}{\Theta}\right)^{n_2} - 1\right]\exp(n_4\ \|\mathbf{C}\|), \tag{40}$$

where n_1, n_2, n_3, and n_4 are temperature parameters that need to be solved through the parameter identification process. Note that at Θ_0, $g_g^{\mathrm{v}} = 0$ and $g_r^{\mathrm{v}} \approx 1$, which consists with the assumption of $\left[\frac{\Theta}{\Theta_0} + g^{\mathrm{v}}\right] = 1$ at the reference temperature before. The form of $\phi(\lambda, \Theta)$ in Eq. (32) is finally written as

$$\begin{aligned}\phi(\lambda,\Theta) = {} & \frac{3n_3n_4}{2}\left[-\tanh(\Theta - T_{\mathrm{g}}) + 1\right]\left[\left(\frac{\Theta_0}{\Theta}\right)^{n_2} - 1\right] \\ & \times \frac{\exp\left(n_4\sqrt{\lambda^4 + \frac{2}{\lambda^2}}\right)}{\sqrt{\lambda^4 + \frac{2}{\lambda^2}}}\left(\lambda^3 - \frac{1}{\lambda^3}\right).\end{aligned} \tag{41}$$

Note that at the reference temperature, $\phi(\lambda, \Theta_0) = 0$.

The stress–strain curves under different temperatures are used to obtain the temperature parameters while the hyperelastic and viscoelastic parameters listed in Tables 4 and 5 are kept frozen. The simulated results are shown in Figs. 23(a) and 23(b) and the corresponding temperature parameters are listed in Table 6. Although there are some deviations compared to the results obtained from the modular approach (see Fig. 15), the general simulated results are satisfactory.

4.6. Model validation

So far, all hyperelastic, viscoelastic, and temperature-dependent parameters have been identified using different sets of experimental data. Now, the identified parameters appearing in the model need to be verified with different sets of data that are not used in the parameter identification process. For instance, Fig. 24 depicts the validation results under uniaxial loading–unloading tension experiments at different maximum strain levels and various temperature conditions. The graphs capture stress–strain nonlinearities at finite deformations, hysteric changes, and temperature sensitivity of the responses quite well.

Quantitatively speaking, the comparison between experimental data and simulated results of the dissipation energy density, Young's modulus, peak stress, and residual strain are plotted, as shown in Fig. 25. Note that the slope of the initial linear part of the stress–strain curve (see Fig. 23(a)) is used as Young's modulus at the strain range of 0 to 0.01. The dissipation energy density and peak stress are simulated well while minor deviations can be seen in the figures for Young's modulus and residual strain, especially during low-temperature conditions. We believe that a more complex expression of g^{v} will help solving these questions. However, since the experimental data has already been simulated well, we do not pursue a precise but complex g^{v}.

4.7. Analysis of the temperature effects

As mentioned above, the scaling function g^{v} is not only related to the temperature field but also to the strain level, especially for the low-temperature case. Combined with the experimental data and constitutive model, contour maps depicting the factor affected by temperature and strain are drawn, as shown in Fig. 26, where the blue colour indicates a lower level while the red indicates a higher value. Note that the so-called "temperature factor" is the ratio of stress levels

Table 5
Viscoelastic parameters.

τ_{11} [s]	τ_{12} [s]	k_1 [s]	τ_{21} [s]	τ_{22} [s]	k_2 [s]	d [MPa]	e [MPa]
9.94891e−2	1.17966e+1	1.75930e+1	5.24140e+0	3.99124e+2	1.97795e+2	3.75859e−2	4.40926e−2

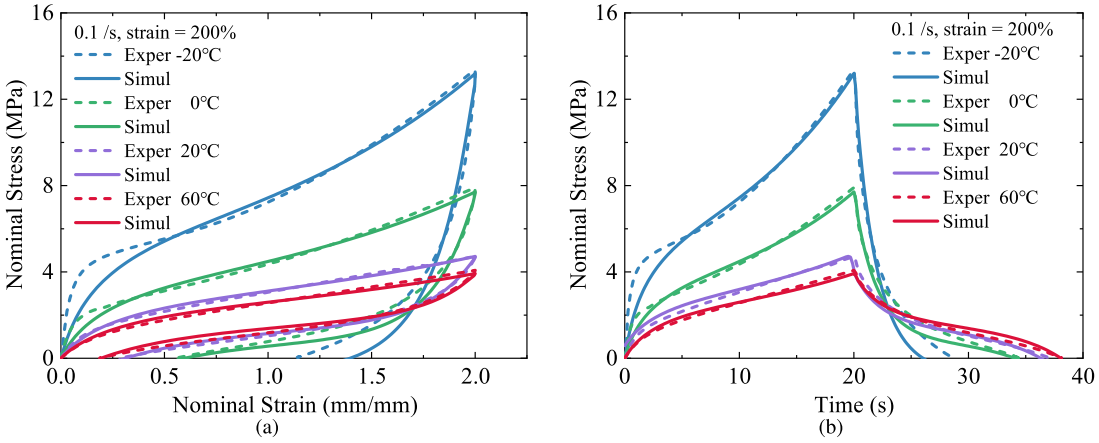

Fig. 23. Thermodynamically-consistent model: general uniaxial tension experiments under different temperatures are carried out to obtain the temperature data. The results are shown in (a) stress–strain and (b) stress–time graphs. Note that the short dashed lines are the experiment data, and the solid lines are the simulated results.

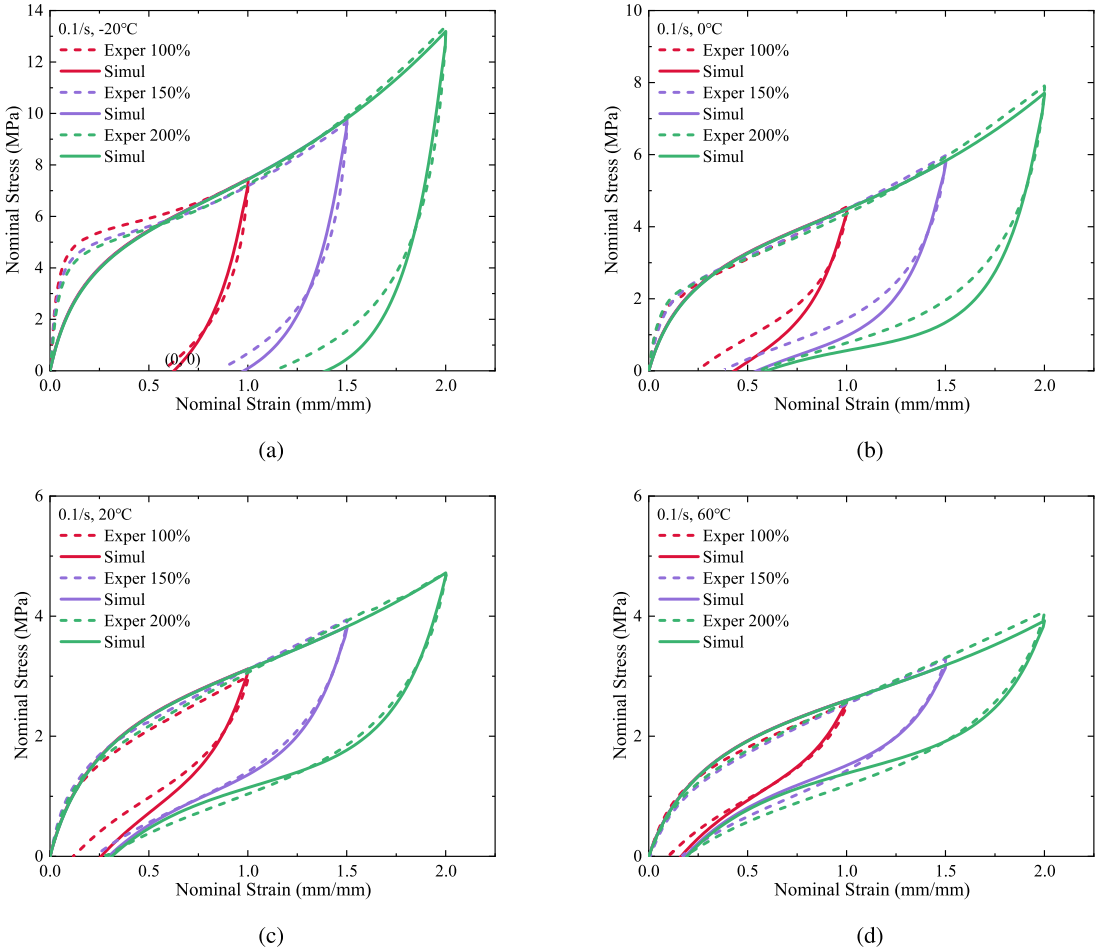

Fig. 24. Validation using uniaxial loading–unloading tension experiments at different strain levels under (a) −20 °C, (b) 0 °C, (c) 20 °C, and (d) 60 °C. The model nicely captures a wide range of experimental data that are not used in the parameter identification process.

at each temperature to that at the reference temperature. It is a similar strategy to Eq. (1).

For the temperature $\Theta \geq 20$ °C, the map in Fig. 26(b) is filled with blue and shows a linear variation with temperature regardless

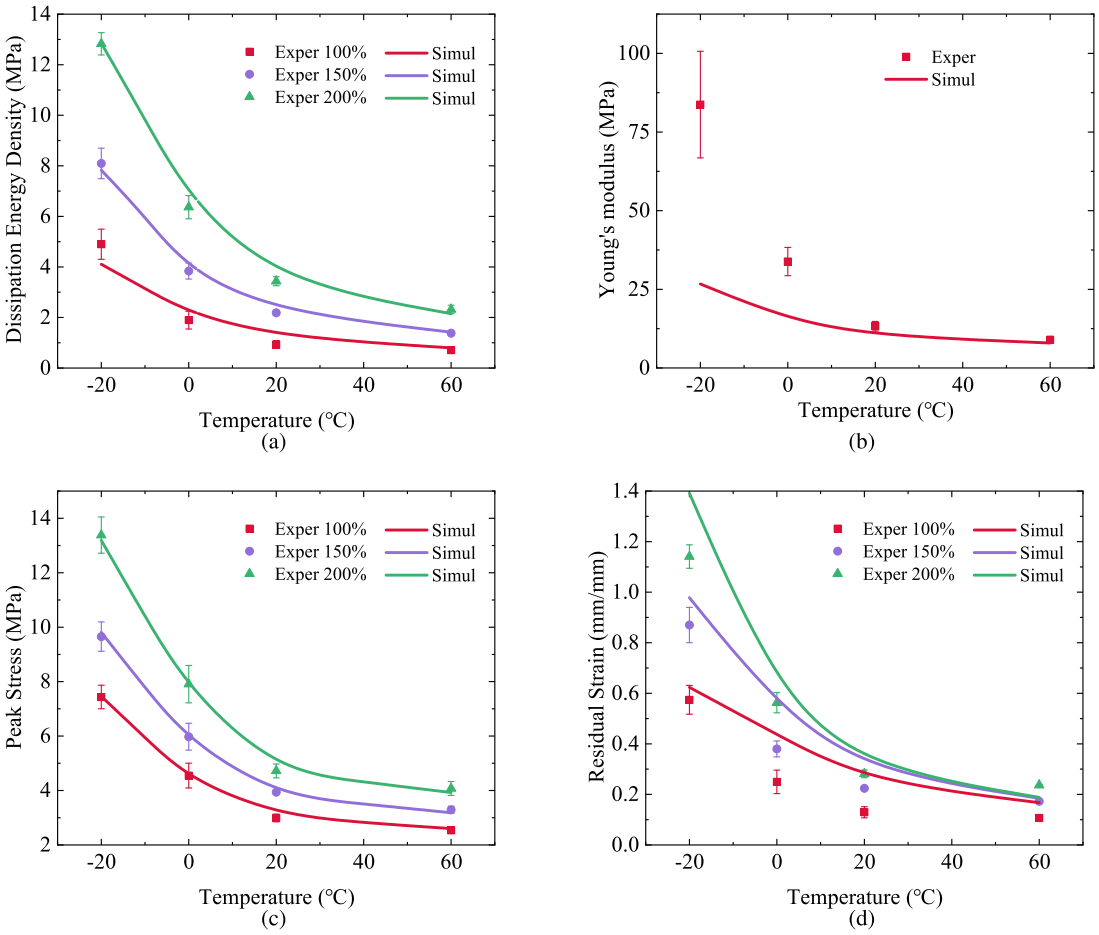

Fig. 25. The variations of (a) dissipation energy density, (b) Young's modulus, (c) peak stress, and (d) residual strain upon the change with temperatures. The symbols mean the experimental results and the solid lines correspond to the simulated results obtained from the constitutive model.

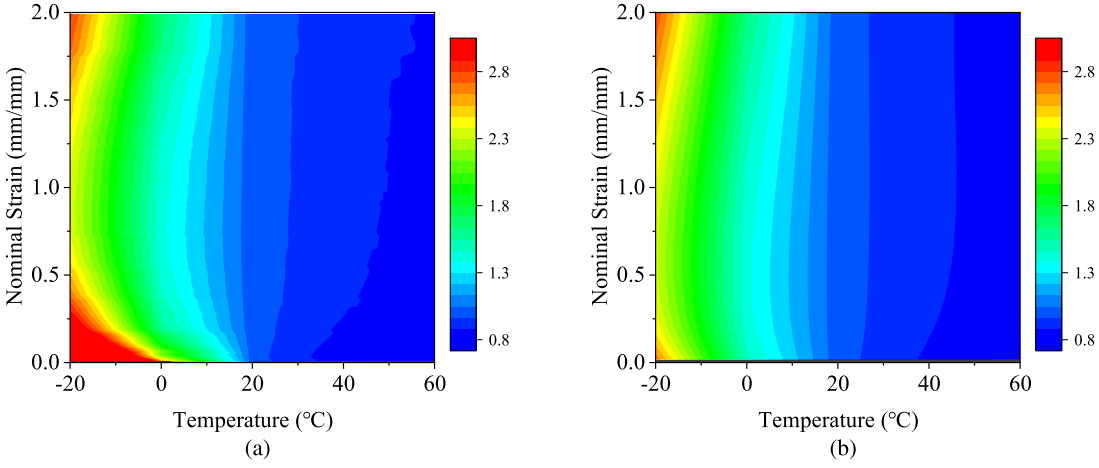

Fig. 26. (a) Experimental and (b) simulated contour maps of temperature factor as a function of temperature and strain level reflecting the influence extent to the stress from temperature effect. For $\Theta \geq 20$ °C, temperature factor shows a linear variation with the change of temperature almost regardless of strain. For $\Theta \leq 20$ °C, temperature factor is not only influenced by temperature, but also by strain level, reflecting a high nonlinear response of temperature effect to the stress values at the glass state.

Table 6
Temperature parameters.

n_1 [–]	n_2 [–]	n_3 [–]	n_4 [–]
3.19422e+0	1.44167e−3	1.67023e+4	2.99621e−2

of strain. This means that the temperature factor is mostly affected by temperature variations at the rubbery state, which is very close to the experimental results, as seen in Fig. 26(a). In our previous study, a scaling parameter with a linear variation was successfully used to describe the stress evolution under different temperatures of the rubbery state (Liao et al., 2020b).

For the temperature $\Theta \leq 20$ °C, after the glass transition occurs, the nominal stress during the tensile loading process increases rapidly with the decrease in temperature in the experiments, as shown in Fig. 10.

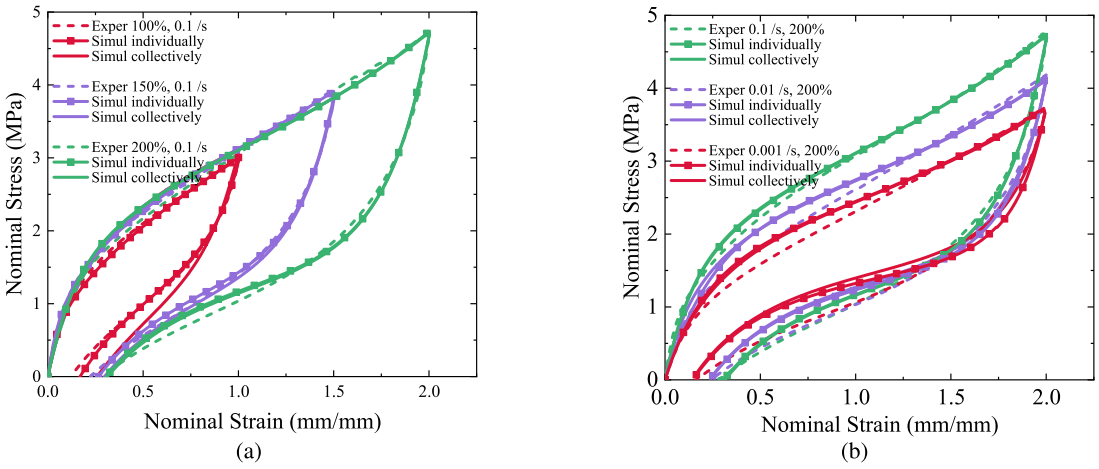

Fig. 27. Stress–strain curves of loading–unloading tests at (a) different strain levels and at (b) different strain rates of experiments and two kinds of simulated schemes at 20 °C.

As mentioned before, temperature dependence is correlated with strain levels. This regularity can be seen in Fig. 26(a), which shows strong nonlinearity and temperature-strain-dependence of the factor. It should be noted that since this model cannot capture the initial stage perfectly, e.g., the deviation of Young's modulus between experimental data and simulated results (see Fig. 25(b)), the maximum value in Fig. 26(b) do not lie in the initial stage where it should be like the style shown in Fig. 26(a). However, the model developed here still shows reliability since the experimental data has been simulated well. In addition, the strain rate is also a dominant effect on the stress–strain relationship. Investigation about this will be carried out in the future.

4.8. Analysis of the internal variables

During the viscoelastic parameter identification process, normally, data under different strain rates (e.g., 0.1 /s, 0.01 /s, and 0.001 /s) should be used collectively to identify a single set of viscoelastic parameters (see Table 5). However, we cannot tell how the internal variables evolve from the experimental results. Therefore, we try to obtain exact simulations of each experiment at a certain loading rate and maximum strain level with an individual set of parameters (experiments at different conditions are fitted with different sets of parameters), using the same model. This fitting gives us a reference of the internal variable that produces the stress response very close to the experimental results, which the collective simulation can compare to. For distinction, we title them "simulated collectively" and "simulated individually", respectively. In addition, we assume that the latter indicates the actual evolution of internal variables while "simulated collectively" introduces the evolution of our model.

Specifically speaking, the results of the experiments, "simulated individually", and "simulated collectively" are plotted under different maximum strain levels (see Fig. 27(a)) and different strain rates (see Fig. 27(b)). As expected, it can be seen that the results of the "simulated individually" are very close to the experimental data. The trends of λ_j^{v} are then extracted from the model, and the results are plotted versus time under different maximum strain levels (see Figs. 28(a) and 28(b)) and different strain rates (see Figs. 28(c) and 28(d)). Inside these figures, the grey dotted lines represent the ending of loading processes under each loading condition, that is, the peak stress points in the corresponding loading and unloading curves. From these four figures, we can find the regularity of the evolution trends of λ_j^{v} under different conditions, i.e., roughly linearly dependent on the maximum strain levels and the strain rates. More specifically, as the maximum strain level and/or strain rate increases, the peaks of λ_1^{v} and λ_2^{v} increase. The differences lie in the slopes of the curves corresponding to loading processes in different loading conditions. In the case of different maximum strain levels, the figures keep similar slopes, while in the other case, the slopes are positively correlated to the logarithmic value of rate accordingly. From the evolutions, we also conclude that at a lower maximum strain level and lower loading rate, the value of λ_j^{v} is smaller, which corresponds to a smaller viscous stress level. This theoretically explains the susceptibility of the thermo-mechanical properties of soft materials to loading conditions. It is also worth mentioning that the grey lines do not coincide with the λ_j^{v} peak moment in each curve, which means the existence of the strain lag effect. For soft polymers, this may result from the internal friction between chain segments during stretching process.

5. Conclusion

This contribution investigates the thermo-viscoelastic responses of the DLS-based digitally-printed EPU polymer under the effects of various temperature conditions followed by developing a constitutive modelling framework and its experimental validation. A systematic viscoelastic test including uniaxial tensile loading–unloading cyclic tests, single and multi-step relaxation tests under different temperature fields ranging from −20 °C to 60 °C are performed. All temperatures are selected around the glass transition range so that the transition can be observed in the experiments. The polymer demonstrates a high temperature-sensitive behaviour while an extreme nonlinearity of the stress–strain responses at finite deformations can be seen in the experimental study. To explore the temperature effects, we compare the normalised stress levels at different temperatures. Results show that the temperature dependence is also correlated with strain levels. Motivated by the experimental results, a thermodynamically-consistent phenomenologically-inspired constitutive model is built based on continuum mechanics at finite deformations. To the end, the Carroll model is used to describe the equilibrium part of the total stress, and a viscoelastic energy function is used for the non-equilibrium part. To reflect the temperature effect, the stress contributed by viscoelasticity is amplified by a temperature-strain coupling parameter. The results reveal that the model can represent the extreme nonlinearity in the stress–strain relationships and temperature-dependency during mechanical stretching experiments. Its ability to represent the mechanical properties of glassy and rubbery states demonstrates the practicability of our constitutive model. Two contour maps as a function of temperature and strain are also drawn to help understand the temperature variation profile more clearly during stretching deformation. In addition, we analyse the evolution of internal variables and theoretically explain the sensitivity of thermo-mechanical properties of EPU to loading conditions as well as the strain lag effect of our model. The experimental approach and the constitutive modelling framework developed in this manuscript can be broadly applied to study other 3D-printed soft polymers. Considering

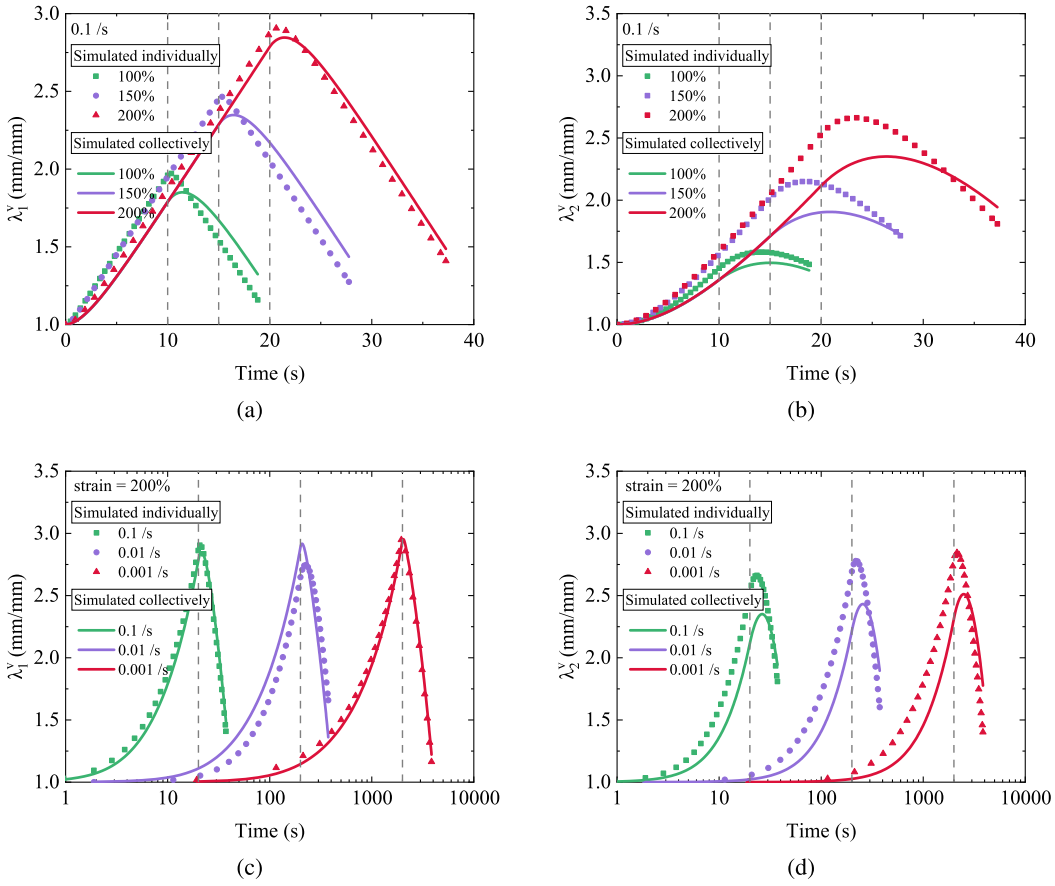

Fig. 28. Evolution of λ_1^v and λ_2^v under different maximum strain levels at the strain rate of 0.1 /s ((a) & (b)) and different strain rates at the strain of 200% ((c) & (d)).

the innovatory technology of DLS, future studies are planned to reveal more detailed microstructural mechanisms (e.g., the ratio of hard to soft domains), as well as the dynamical response of digitally-printed polymers.

Declaration of competing interest

The authors declare that they have no known competing financial interests or personal relationships that could have appeared to influence the work reported in this paper.

Data availability

Data will be made available on request.

Acknowledgements

This study is funded by the Swansea Bay City Deal, United Kingdom and the European Regional Development Fund through the Welsh European Funding Office. This study is also supported by EPSRC through the Supergen ORE Hub (EP/S000747/1), who have awarded funding for the Flexible Fund project Submerged bi-axial fatigue analysis for flexible membrane Wave Energy Converters (FF2021-1036). This work is partially supported by the National Science Fund for Distinguished Young Scholar, China (No. 11925203), the National Natural Science Foundation of China (No. 11672110), and the Open Project Program of State Key Laboratory of Traction Power, China under Grant (No. TPL2003). A. SM Alzaidi acknowledges Taif University Researchers, Saudi Arabia Supporting Project number (TURSP-2020/303), Taif University, Taif, Saudi Arabia.

References

Abali, B.E., Barchiesi, E., 2021. Additive manufacturing introduced substructure and computational determination of metamaterials parameters by means of the asymptotic homogenization. Contin. Mech. Thermodyn. 33 (4), 993–1009. http://dx.doi.org/10.1007/s00161-020-00941-w.

Akindoyo, J.O., Beg, M.D.H., Ghazali, S., Islam, M.R., Jeyaratnam, N., Yuvaraj, A.R., 2016. Polyurethane types, synthesis and applications – a review. RSC Adv. 6 (115), 114453–114482. http://dx.doi.org/10.1039/C6RA14525F.

Al Rashid, A., Ahmed, W., Khalid, M., Koca, M., 2021. Vat photopolymerization of polymers and polymer composites: Processes and applications. Addit. Manuf. 21, 102279. http://dx.doi.org/10.1016/j.addma.2021.102279.

Amirkhizi, A.V., Isaacs, J., McGee, J., Nemat-Nasser, S., 2006. An experimentally-based viscoelastic constitutive model for polyurea, including pressure and temperature effects. Phil. Mag. 86 (36), 5847–5866. http://dx.doi.org/10.1080/14786430600833198.

Arman, B., Reddy, A.S., Arya, G., 2012. Viscoelastic properties and shock response of coarse-grained models of multiblock versus diblock copolymers: Insights into dissipative properties of polyurea. Macromolecules 45 (7), 3247–3255. http://dx.doi.org/10.1021/ma3001934.

Arruda, E.M., Boyce, M.C., 1993. A three-dimensional constitutive model for the large stretch behavior of rubber elastic materials. J. Mech. Phys. Solids 41 (2), 389–412. http://dx.doi.org/10.1016/0022-5096(93)90013-6.

Associates, W. (Ed.), 2016. Wohlers Report 2016: 3D Printing and Additive Manufacturing State of the Industry Annual Worldwide Progress Report. Wohlers Associates, Fort Collins (Colo.).

Chattopadhyay, D., Raju, K., 2007. Structural engineering of polyurethane coatings for high performance applications. Prog. Polym. Sci. 32 (3), 352–418. http://dx.doi.org/10.1016/j.progpolymsci.2006.05.003.

Cho, H., Rinaldi, R.G., Boyce, M.C., 2013. Constitutive modeling of the rate-dependent resilient and dissipative large deformation behavior of a segmented copolymer polyurea. Soft Matter 9 (27), 6319. http://dx.doi.org/10.1039/c3sm27125k.

Christ, J.F., Aliheidari, N., Ameli, A., Pötschke, P., 2017. 3D printed highly elastic strain sensors of multiwalled carbon nanotube/thermoplastic polyurethane nanocomposites. Mater. Des. 131, 394–401. http://dx.doi.org/10.1016/j.matdes.2017.06.011.

Christ, J., Aliheidari, N., Pötschke, P., Ameli, A., 2018. Bidirectional and stretchable piezoresistive sensors enabled by multimaterial 3D printing of carbon nanotube/thermoplastic polyurethane nanocomposites. Polymers 11 (1), 11. http://dx.doi.org/10.3390/polym11010011.

Clifton, R.J., Wang, X., Jiao, T., 2016. A physically-based, quasilinear viscoelasticity model for the dynamic response of polyurea. J. Mech. Phys. Solids 93, 8–15. http://dx.doi.org/10.1016/j.jmps.2016.04.027.

Ding, F., Liu, T., Zhang, H., Liu, L., Li, Y., 2021. Stress-strain curves for polyurethane elastomers: A statistical assessment of constitutive models. J. Appl. Polym. Sci. 138 (39), 51269. http://dx.doi.org/10.1002/app.51269.

Dippel, B., Johlitz, M., Lion, A., 2015. Thermo-mechanical couplings in elastomers - experiments and modelling: Thermo-mechanical couplings in elastomers - experiments and modelling. ZAMM - J. Appl. Math. Mech. / Z. Angew. Math. Mech. 95 (11), 1117–1128. http://dx.doi.org/10.1002/zamm.201400110.

Dorfmann, A., Ogden, R., 2004. A constitutive model for the Mullins effect with permanent set in particle-reinforced rubber. Int. J. Solids Struct. 41 (7), 1855–1878. http://dx.doi.org/10.1016/j.ijsolstr.2003.11.014.

Dorfmann, A., Trimmer, B., Woods, W., 2007. A constitutive model for muscle properties in a soft-bodied arthropod. J. R. Soc. Interface 4 (13), 257–269. http://dx.doi.org/10.1098/rsif.2006.0163.

Garzon-Hernandez, S., Arias, A., Garcia-Gonzalez, D., 2020a. A continuum constitutive model for FDM 3D printed thermoplastics. Composites B 201, 108373. http://dx.doi.org/10.1016/j.compositesb.2020.108373.

Garzon-Hernandez, S., Garcia-Gonzalez, D., Jerusalem, A., Arias, A., 2020b. Design of FDM 3D printed polymers: An experimental-modelling methodology for the prediction of mechanical properties. Mater. Des. 188, 108414. http://dx.doi.org/10.1016/j.matdes.2019.108414.

Gong, C., Chen, Y., Li, T., Liu, Z., Zhuang, Z., Guo, B., Wang, H., Dai, L., 2021. Free volume based nonlinear viscoelastic model for polyurea over a wide range of strain rates and temperatures. Mech. Mater. 152, 103650. http://dx.doi.org/10.1016/j.mechmat.2020.103650.

Grujicic, M., He, T., Pandurangan, B., Runt, J., Tarter, J., Dillon, G., 2011. Development and parameterization of a time-invariant (equilibrium) material model for segmented elastomeric polyureas. Proc. Inst. Mech. Eng., L 225 (3), 182–194. http://dx.doi.org/10.1177/0954420711401959.

Guo, H., Guo, W., Amirkhizi, A.V., Zou, R., Yuan, K., 2016. Experimental investigation and modeling of mechanical behaviors of polyurea over wide ranges of strain rates and temperatures. Polym. Test. 53, 234–244. http://dx.doi.org/10.1016/j.polymertesting.2016.06.004.

Holzapfel, G.A., 2000. Nonlinear Solid Mechanics: A Continuum Approach for Engineering. Wiley, Chichester;New York.

Hossain, M., Liao, Z., 2020. An additively manufactured silicone polymer: Thermo-viscoelastic experimental study and computational modelling. Addit. Manuf. 35, 101395. http://dx.doi.org/10.1016/j.addma.2020.101395.

Hossain, M., Navaratne, R., Perić, D., 2020. 3D printed elastomeric polyurethane: Viscoelastic experimental characterizations and constitutive modelling with nonlinear viscosity functions. Int. J. Non-Linear Mech. 126, 103546. http://dx.doi.org/10.1016/j.ijnonlinmec.2020.103546.

Jiao, T., Clifton, R.J., Grunschel, S.E., 2009. Pressure-sensitivity and constitutive modeling of an elastomer at high strain rates. AIP Conf. Proc. 1195 (1), 1229–1232. http://dx.doi.org/10.1063/1.3295026.

Kim, Y.C., Hong, S., Sun, H., Kim, M.G., Choi, K., Cho, J., Choi, H.R., Koo, J.C., Moon, H., Byun, D., Kim, K.J., Suhr, J., Kim, S.H., Nam, J.-D., 2017. UV-curing kinetics and performance development of in situ curable 3D printing materials. Eur. Polym. J. 93, 140–147. http://dx.doi.org/10.1016/j.eurpolymj.2017.05.041.

Koprowski-Theiss, N., Johlitz, M., Diebels, S., 2011. Characterizing the time dependence of filled epdm. Rubber Chem. Technol. 84 (2), 147–165. http://dx.doi.org/10.5254/1.3570527.

Krol, P., 2007. Synthesis methods, chemical structures and phase structures of linear polyurethanes. Properties and applications of linear polyurethanes in polyurethane elastomers, copolymers and ionomers. Prog. Mater. Sci. 52 (6), 915–1015. http://dx.doi.org/10.1016/j.pmatsci.2006.11.001.

Larcher, M., Solomos, G., Casadei, F., Gebbeken, N., 2012. Experimental and numerical investigations of laminated glass subjected to blast loading. Int. J. Impact Eng. 39 (1), 42–50. http://dx.doi.org/10.1016/j.ijimpeng.2011.09.006.

Liao, Z., Hossain, M., Yao, X., 2020a. Ecoflex polymer of different shore hardnesses: Experimental investigations and constitutive modelling. Mech. Mater. 144, 103366. http://dx.doi.org/10.1016/j.mechmat.2020.103366.

Liao, Z., Hossain, M., Yao, X., Mehnert, M., Steinmann, P., 2020b. On thermo-viscoelastic experimental characterization and numerical modelling of VHB polymer. Int. J. Non-Linear Mech. 118, 103263. http://dx.doi.org/10.1016/j.ijnonlinmec.2019.103263.

Liao, Z., Yang, J., Hossain, M., Chagnon, G., Jing, L., Yao, X., 2021. On the stress recovery behaviour of Ecoflex silicone rubbers. Int. J. Mech. Sci. 206, 106624. http://dx.doi.org/10.1016/j.ijmecsci.2021.106624.

Liao, Z., Yao, X., Zhang, L., Hossain, M., Wang, J., Zang, S., 2019. Temperature and strain rate dependent large tensile deformation and tensile failure behavior of transparent polyurethane at intermediate strain rates. Int. J. Impact Eng. 129, 152–167. http://dx.doi.org/10.1016/j.ijimpeng.2019.03.005.

Ligon, S.C., Liska, R., Stampfl, J., Gurr, M., Mülhaupt, R., 2017. Polymers for 3D Printing and customized additive manufacturing. Chem. Rev. 117 (15), 10212–10290. http://dx.doi.org/10.1021/acs.chemrev.7b00074.

Lion, A., 1997. A physically based method to represent the thermo-mechanical behaviour of elastomers. Acta Mech. 123 (1–4), 1–25. http://dx.doi.org/10.1007/bf01178397.

Lu, S., Pister, K., 1975. Decomposition of deformation and representation of the free energy function for isotropic thermoelastic solids. Int. J. Solids Struct. 11 (7–8), 927–934. http://dx.doi.org/10.1016/0020-7683(75)90015-3.

Mehnert, M., Hossain, M., Steinmann, P., 2021. A complete thermo-electro-viscoelastic characterization of dielectric elastomers, Part II: Continuum modeling approach. J. Mech. Phys. Solids 157, 104625. http://dx.doi.org/10.1016/j.jmps.2021.104625.

Nantasetphong, W., Amirkhizi, A., Nemat-Nasser, S., 2016. Constitutive modeling and experimental calibration of pressure effect for polyurea based on free volume concept. Polymer 99, 771–781. http://dx.doi.org/10.1016/j.polymer.2016.07.071.

Nikoukalam, M., Sideris, P., 2019. Experimental characterization and constitutive modeling of polyurethanes for structural applications, accounting for damage, hysteresis, loading rate and long term effects. Eng. Struct. 198, 109462. http://dx.doi.org/10.1016/j.engstruct.2019.109462.

Park, S., Moon, J., Kim, B., Cho, M., 2021. Multi-scale coarse-grained molecular dynamics simulation to investigate the thermo-mechanical behavior of shape-memory polyurethane copolymers. Polymer 213, 123228. http://dx.doi.org/10.1016/j.polymer.2020.123228.

Petrović, Z.S., Ferguson, J., 1991. Polyurethane elastomers. Prog. Polym. Sci. 16 (5), 695–836. http://dx.doi.org/10.1016/0079-6700(91)90011-9.

Pramanik, R., Soni, F., Shanmuganathan, K., Arockiarajan, A., 2022. Mechanics of soft polymeric materials using a fractal viscoelastic model. Mech. Time-Dependent Mater. 26 (2), 257–270. http://dx.doi.org/10.1007/s11043-021-09486-0.

Qi, H., 2004. Constitutive model for stretch-induced softening of the stress-stretch behavior of elastomeric materials. J. Mech. Phys. Solids 52 (10), 2187–2205. http://dx.doi.org/10.1016/j.jmps.2004.04.008.

Qi, H., Boyce, M., 2005a. Stress–Strain behavior of thermoplastic polyurethanes. Mech. Mater. 37 (8), 817–839. http://dx.doi.org/10.1016/j.mechmat.2004.08.001.

Qi, H., Boyce, M., 2005b. Stress–Strain behavior of thermoplastic polyurethanes. Mech. Mater. 37 (8), 817–839. http://dx.doi.org/10.1016/j.mechmat.2004.08.001.

Rafiee, Z., Keshavarz, V., 2015. Synthesis and characterization of polyurethane/microcrystalline cellulose bionanocomposites. Prog. Org. Coat. 86, 190–193. http://dx.doi.org/10.1016/j.porgcoat.2015.05.013.

Reese, S., Govindjee, S., 1997. Theoretical and numerical aspects in the thermo-viscoelastic material behaviour of rubber-like polymers. Mech. Time-Dependent Mater. 1 (4), 357–396. http://dx.doi.org/10.1023/A:1009795431265.

Reese, S., Govindjee, S., 1998. A theory of finite viscoelasticity and numerical aspects. Int. J. Solids Struct. 35 (26–27), 3455–3482. http://dx.doi.org/10.1016/s0020-7683(97)00217-5.

Rull, N., Basnayake, A., Heitzmann, M., Frontini, P.M., 2021. Constitutive modelling of the mechanical response of a polycaprolactone based polyurethane elastomer: Finite element analysis and experimental validation through a bulge test. J. Strain Anal. Eng. Des. 56 (4), 206–215. http://dx.doi.org/10.1177/0309324720958332.

Sarva, S.S., Deschanel, S., Boyce, M.C., Chen, W., 2007. Stress–Strain behavior of a polyurea and a polyurethane from low to high strain rates. Polymer 48 (8), 2208–2213. http://dx.doi.org/10.1016/j.polymer.2007.02.058.

Scheffer, T., Goldschmidt, F., Diebels, S., 2015. Implementation of the strongly pronounced non-linear viscoelasticity of an incompressible filled rubber. In: Technische Mechanik. (ISSN: 2199-9244) pp. 119–132. http://dx.doi.org/10.24352/ub.ovgu-2017-074, 35; 2; 0, 33 MB.

Shim, J., Mohr, D., 2011. Rate dependent finite strain constitutive model of polyurea. Int. J. Plast. 27 (6), 868–886. http://dx.doi.org/10.1016/j.ijplas.2010.10.001.

Slesarenko, V., Rudykh, S., 2018. Towards mechanical characterization of soft digital materials for multimaterial 3D-printing. Internat. J. Engrg. Sci. 123, 62–72. http://dx.doi.org/10.1016/j.ijengsci.2017.11.011.

Somarathna, H., Raman, S., Mohotti, D., Mutalib, A., Badri, K., 2020a. Hyper-viscoelastic constitutive models for predicting the material behavior of polyurethane under varying strain rates and uniaxial tensile loading. Constr. Build. Mater. 236, 117417. http://dx.doi.org/10.1016/j.conbuildmat.2019.117417.

Somarathna, H., Raman, S., Mohotti, D., Mutalib, A., Badri, K., 2020b. Rate dependent tensile behavior of polyurethane under varying strain rates. Constr. Build. Mater. 254, 119203. http://dx.doi.org/10.1016/j.conbuildmat.2020.119203.

Stansbury, J.W., Idacavage, M.J., 2016. 3D printing with polymers: Challenges among expanding options and opportunities. Dent. Mater. 32 (1), 54–64. http://dx.doi.org/10.1016/j.dental.2015.09.018.

Tumbleston, J.R., Shirvanyants, D., Ermoshkin, N., Janusziewicz, R., Johnson, A.R., Kelly, D., Chen, K., Pinschmidt, R., Rolland, J.P., Ermoshkin, A., Samulski, E.T., DeSimone, J.M., 2015. Continuous liquid interface production of 3D objects. Science 347 (6228), 1349–1352. http://dx.doi.org/10.1126/science.aaa2397.

Unkovskiy, A., Spintzyk, S., Brom, J., Huettig, F., Keutel, C., 2018. Direct 3D printing of silicone facial prostheses: A preliminary experience in digital workflow. J. Prosthet. Dent. 120 (2), 303–308. http://dx.doi.org/10.1016/j.prosdent.2017.11.007.

Vyas, A., Garg, V., Ghosh, S.B., Bandyopadhyay-Ghosh, S., 2022. Photopolymerizable resin-based 3D printed biomedical composites: Factors affecting resin viscosity. In: Materials Today-Proceedings, Vol. 62. pp. 1435–1439. http://dx.doi.org/10.1016/j.matpr.2022.01.172.

Wang, Y., Luo, W., Huang, J., Peng, C., Wang, H., Yuan, C., Chen, G., Zeng, B., Dai, L., 2020. Simplification of hyperelastic constitutive model and finite element analysis of thermoplastic polyurethane elastomers. Macromol. Theory Simul. 29 (4), 2000009. http://dx.doi.org/10.1002/mats.202000009.

Wang, C., Wang, R., Xu, Y., Zhang, M., Yang, F., Sun, S., Zhao, C., 2017. A facile way to prepare anti-fouling and blood-compatible polyethersulfone membrane via blending with heparin-mimicking polyurethanes. Mater. Sci. Eng.: C 78, 1035–1045. http://dx.doi.org/10.1016/j.msec.2017.04.123.

Xiang, Y., Schilling, C., Arora, N., Boydston, A., Rudykh, S., 2020. Mechanical characterization and constitutive modeling of visco-hyperelasticity of photocured polymers. Addit. Manuf. 36, 101511. http://dx.doi.org/10.1016/j.addma.2020.101511.

Xiao, R., Han, N., Zhong, D., Qu, S., 2021. Modeling the mechanical behaviors of multiple network elastomers. Mech. Mater. 161, 103992. http://dx.doi.org/10.1016/j.mechmat.2021.103992.

Yang, J., Custer, D., Chiang, C.C., Meng, Z., Yao, X., 2021. Understanding the mechanical and viscoelastic properties of graphene reinforced polycarbonate nanocomposites using coarse-grained molecular dynamics simulations. Comput. Mater. Sci. 191, 110339. http://dx.doi.org/10.1016/j.commatsci.2021.110339.

Yang, J., Yao, X., Meng, Z., 2022. Investigation of molecular mechanisms of polyvinylidene fluoride under the effects of temperature, electric poling, and mechanical stretching using molecular dynamics simulations. Polymer 124691. http://dx.doi.org/10.1016/j.polymer.2022.124691.

Yi, J., Boyce, M., Lee, G., Balizer, E., 2006. Large deformation rate-dependent Stress–Strain behavior of polyurea and polyurethanes. Polymer 47 (1), 319–329. http://dx.doi.org/10.1016/j.polymer.2005.10.107.

Yousaf, Z., Smith, M., Potluri, P., Parnell, W., 2020. Compression properties of polymeric syntactic foam composites under cyclic loading. Composites B 186, 107764. http://dx.doi.org/10.1016/j.compositesb.2020.107764.

Yu, K., Xin, A., Wang, Q., 2019. Mechanics of light-activated self-healing polymer networks. J. Mech. Phys. Solids 124, 643–662. http://dx.doi.org/10.1016/j.jmps.2018.11.019.

Yuan, Y., Wang, S., Tan, P., Zhu, H., 2020. Mechanical performance and shear constitutive model study of a new high-capacity polyurethane elastomeric bearing. Constr. Build. Mater. 232, 117227. http://dx.doi.org/10.1016/j.conbuildmat.2019.117227.

Zhang, M., Cui, Z., Catherine Brinson, L., 2018. Mechanical properties of hard-soft block copolymers calculated from coarse-grained molecular dynamics models. J. Polym. Sci. B: Polym. Phys. 56 (23), 1552–1566. http://dx.doi.org/10.1002/polb.24742.

Zhang, X., Hao, H., Shi, Y., Cui, J., 2015a. The mechanical properties of Polyvinyl Butyral (PVB) at high strain rates. Constr. Build. Mater. 93, 404–415. http://dx.doi.org/10.1016/j.conbuildmat.2015.04.057.

Zhang, X., Wang, J., Guo, W., Zou, R., 2017. A bilinear constitutive response for polyureas as a function of temperature, strain rate and pressure. J. Appl. Polym. Sci. 134 (35), 45256. http://dx.doi.org/10.1002/app.45256.

Zhang, L., Yao, X., Zang, S., Gu, Y., 2015b. Temperature- and strain rate-dependent constitutive modeling of the large deformation behavior of a transparent polyurethane interlayer. Polym. Eng. Sci. 55 (8), 1864–1872. http://dx.doi.org/10.1002/pen.24026.

Zhang, L., Yao, X., Zang, S., Han, Q., 2015c. Temperature and strain rate dependent tensile behavior of a transparent polyurethane interlayer. Mater. Des. (1980-2015) 65, 1181–1188. http://dx.doi.org/10.1016/j.matdes.2014.08.054.

Zhang, L., Zhang, X., Yao, X., Zang, S., 2015d. Experimental investigation on the tensile behavior of a transparent polyurethane interlayer. Int. J. Mater. Res. 106 (9), 996–1001. http://dx.doi.org/10.3139/146.111267.

Zhao, Z., Mu, X., Sowan, N., Pei, Y., Bowman, C.N., Jerry Qi, H., Fang, D., 2015. Effects of oxygen on light activation in covalent adaptable network polymers. Soft Matter 11 (30), 6134–6144. http://dx.doi.org/10.1039/C5SM00555H.

Zhou, Y., Wang, F., Yang, Z., Hu, X., Pan, Y., Lu, Y., Jiang, M., 2022. 3D printing of polyurethane/nanocellulose shape memory composites with tunable glass transition temperature. Ind. Crop. Prod. 182, 114831. http://dx.doi.org/10.1016/j.indcrop.2022.114831.